2015

Unconventional elastomeric microsystems: fabrication and application

Jungwook Paek
Iowa State University

Unconventional elastomeric microsystems: Fabrication and application

by

Jungwook Paek

A dissertation submitted to the graduate faculty

in partial fulfillment of the requirements for the degree of

DOCTOR OF PHILOSOPHY

Major: Electrical Engineering

Program of Study Committee:
Jaeyoun Kim, Major Professor
Vikram Dalal
Jiming Song
Santosh Pandey
Meng Lu

Iowa State University

Ames, Iowa

2015

To my wife, Myungwoon Lee,

I could not have completed this long voyage of my doctoral study without you.

Thank you for your unconditional support and encouragement.

TABLE OF CONTENTS

Page

LIST OF FIGURES v

LIST OF TABLES vii

ACKNOLEDGEMENTS viii

ABSTRACT ix

CHAPTER 1 INTRODUCTION 1
Research Motivations 1
Research Challenges 2
Dissertation Organization 5

CHAPTER 2 SUCROSE BASED FABRICATION OF 3D NETWORKED, CYLINDRICAL MICROFLUIDIC CHANNELS 7
Abstract 7
Introduction 7
Fabrication of 3D-networked, Cylindrical Microfluidic Channels 9
Fabrication Results and Discussion 12
Conclusion 16
Acknowledgements 17

CHAPTER 3 BOKEH MICROSCOPE-INTEGRATED MICROFLUIDIC CHANNELS FOR FACILE POINT-OF-CARE MONITORING 18
Abstract 18
Introduction 18
Bokeh Microscope Design 21
Fabrication of MF Channel-Integrated *Bokeh* Microscope 22
Characterization of *Bokeh* Microscope 26
Conclusion 28
Acknowledgements 28

CHAPTER 4 MICROSPHERE-ASSISTED FABRICATION OF HIGH ASPECT RATIO ELASTOMERIC MICROPILLARS AND WAVEGUIDES 29
Abstract 29
Introduction 30
Fabrication of Microsphere-Tipped PDMS Micropillars 32
Fabrication Results and Impact of the *In Situ* Heating 34
Air-Flow Sensing with Microsphere-Tipped PDMS Micropillars and Discussion 43

Conclusion 55
Acknowledgements 56

CHAPTER 5 MICROROBOTIC TENTACLES WITH SPIRAL BENDING CAPABILITY BASED ON SHAPE-ENGINEERED ELASTIC MICROTUBE.... 57
Abstract 57
Introduction 58
Fabrication of PDMS Microtube based Soft-Robotic Tentacles..... 59
Pneumatic Actuation of PDMS Microtubes 62
Shape-Engineering for Tentacle Motion..... 64
Characterization of Micro-Tentacle Actuation and Discussion 66
Conclusion 72
Acknowledgements 73

CHAPTER 6 SUMMARY AND CONCLUSIONS..... 74

REFERENCES..... 77

LIST OF FIGURES

Page

Figure 1 Schematic outline of the sucrose-based rapid-prototyping process 11

Figure 2 Physical characteristics of sucrose templates 13

Figure 3 Fabrication results of 3D MF channel architectures 15

Figure 4 Vaso-mimetic MF architectures 16

Figure 5 MF channel integrated-*bokeh* microscopy scheme and its operation 20

Figure 6 Fabrication steps for a *bokeh* microscope-integrated microfluidic channel 23

Figure 7 Optical design of *bokeh*-effect-enabling microlens 25

Figure 8 *Bokeh* micrographs obtained with different combinations of f_c and L 27

Figure 9 Fabrication of microsphere-tipped PDMS micropillars and their optical air-flow sensing application 33

Figure 10 Physical characteristics of the fabricated microsphere-tipped PDMS micropillars 36

Figure 11 Micropillar merging as the limiting factor to dense array formation 40

Figure 12 Air-flow sensing with microsphere-tipped, high aspect-ratio PDMS micropillars 46

Figure 13 Optical investigation for a decrease in a bent MSMP's reflection 47

Figure 14 The impact of detector size 47

Figure 15 The change in the micropillar's reflection level as a function of the air-flow velocity 48

Figure 16 Sound sensing with microsphere-tipped, high aspect-ratio PDMS micropillars 50

Figure 17 PDMS microtube tentacle actuator and its fabrication 61

Figure 18 Pneumatic actuation of PDMS microtubes 63

Figure 19 Shape-engineering of PDMS micro-tentacles 67

Figure 20 Changes in the integrands due to the hump 68

Figure 21 Characterization of PDMS micro-tentacle actuation 71

LIST OF TABLES

		Page
Table 1	Imaging characteristics of the camera lens at different f_c values and the corresponding magnification and FoV extent	22
Table 2	Characteristics of the PDMS micropillars under test	35
Table 3	Overall statistics of the height and diameter for the 4 x4 MSMP array shown in Fig. 10b	38
Table 4	Height map of the 4×4 MSMP array	38
Table 5	Diameter map of the 4×4 MSMP array	38
Table 6	Diameters of the microspheres used for the MSMP array fabrication	39

ACKNOWLEDGMENTS

First of all, I would like to express my deepest gratitude to my major professor, Dr. Jaeyoun Kim for his invaluable guidance and constructive feedback throughout the course of this research. His excellent expertise, insight and advice, always keep me heading in the right direction during my four-years-journey for Ph. D. degree. Without his excellent guidance, I could not have done this research work. Especially, I want to attribute the recent illuminations on my research work such as highlights from lots of media sources, to my supervisor, Dr. Jaeyoun Kim's great instruction. I, also, appreciate the guidance and suggestion of my present committee members, Dr. Vikram Dalal, Dr. Jiming Song, Dr. Santosh Pandey, and Dr. Meng Lu, and my formal committee member, Dr. Liang Dong for my research work. I believe that the excellent quality of their graduate classes and expertise gave me great chance to widen my vision relative to research works as well as my academic knowledge so that I could accomplish achievements on diverse research areas.

In addition, I would like to thank my wife, Myungwoon Lee, and my parents for their support and encouragement. Without their unstinting support and backing, my journey to complete this research work has not been possible and satisfying.

Finally, I would also like to extend my thanks to my friends, Sangwook Kang, Eon Kim, Kyuho Lee, Sinyoung Jun and Taejoon Kong for making my time at Iowa State University a wonderful experience.

ABSTRACT

Elastomer-based microsystems hold great promise for a diverse range of applications such as rapid prototyping of lab-on-a-chip device, soft-MEMS, and soft-robotics. For better performance in such applications, unconventional elastomeric structures in terms of size, shape, and patterning trajectory, have been intensely sought after in microtechnology but their realization has been a continuous challenge. Here, as my dissertation work, I present new microfabrication schemes which enable the realizations of unconventional PDMS structures, and their applications, which will enrich the field of soft-microsystems.

First, I present a new fabrication scheme for the realization of cylindrical microfluidic (MF) channels with 3D trajectories based on shaping, bonding, and assembly of sucrose fibers. Due to the high water-solubility of the sucrose templates, the scheme is a simple and environment-friendly. Also, it is cleanroom-free and cost-effective. Despite its simplicity, it enables the realization of essential 3D MF channel architectures such as highly curved MF channels, internal loops, and proper end-to-side junctions. It can, also, realize tapered junctions and stenosis which can benefit vaso-mimetic lab-on-a-chip applications.

Secondly, as a practical application of the sucrose-based MF channel, I report the implementation of the *bokeh*-effect-based microfluidic microscopy scheme for point-of-care health monitoring in highly resource-limited environment. For this work, I integrated a single polymer microlens over the sucrose-templated MF channel and retrieved magnified intra-channel images with a commercial, off-the-shelf camera. The *bokeh* microscope exhibited 10~40 in magnification and 67~252 μm of field-of-view extent, confirming their utility for point-of-care monitoring of micro-scale objects in MF channels

Third, I present a new technique that enables facile fabrications of high aspect-ratio PDMS micropillars exceeding 2400 μm in height and 100 in aspect-ratio. The key enabling factor is the adoption of the direct drawing technique incorporated with the *in situ* heating for simultaneous hardening and solidification of PDMS. The technique also allows self-aligned installation of highly reflective microspheres at the tips of the micropillars. Using the transparent PDMS micropillar as a flexible waveguide and the microsphere as a self-aligned reflector, I transformed the microsphere-tipped PDMS micropillars into all optically interrogated air-flow sensors and successfully demonstrated its air-flow sensing capability.

Lastly, I present a microscale soft-robotic tentacle with spiral bending capability based on pneumatically driven bending motion of a hollow PDMS microtube. For this work, I establish a new, direct peeling-based technique for building long and thin, highly deformable microtubes and a semi-analytical model for their shape-engineering. Based on them, the artificial microrobotic tentacle exhibits the *multi-turn* spiraling motion with the final radius of 185 μm and squeezing force of ~ 0.78 mN. Thanks to the softness of PDMS and the spiraling motion, the micro-tentacle can function as a soft-robotic grabber of fragile micro-objects. The spiraling tentacle-based grabbing modality, the elastomeric microtube fabrication technique, and the concept of microtube shape-engineering will constitute very valuable additions to future microscale soft-robotics.

Here, I organized my dissertation based on four published journal papers of which I am the first/primary author.

CHAPTER 1

INTRODUCTION

Research Motivations

Over the past two decades, poly(dimethylsiloxane) (PDMS) has become the dominant material for fabricating elastomer-based structures such as the microfluidic (MF) channels for rapid prototyping of lab-on-a-chip devices. Recently, the elastomeric structures have seen rapid expansion in their application scope, from their conventional utilizations as MF channels to diverse soft-MEMS devices and soft-robotics by providing new modalities for sensing and actuation. Better performance in such applications, however, demands realizations of PDMS structures unconventionally in terms of size, shape, and patterning trajectory, which is difficult when attempted with conventional fabrication schemes such as replica molding. In response, researchers have continuously explored new fabrication schemes for unconventional PDMS structure fabrication.

Of special interest is the realization of 3D networked [1-3], circular PDMS MF channels [4-6] which try to fill the needs for diverse changes in the architecture of MF channels, beyond their conventional forms of rectangular cross-sections and 2D, planar trajectories. One eminent application of such unconventional MF channels is the vaso-mimetic lab-on-a-chip (LoC) devices in which the MF channels mimic biological vasculatures for tissue scaffolding [7-9] and controlled hemodynamic studies [10-12] in 3D environments.

Other outcomes of such unconventional PDMS structure fabrication efforts [13] include microwires [14-18], beaded wires [19, 20], cantilevers [21], and high aspect-ratio

micropillars. In particular, high aspect-ratio PDMS micropillars have seen rapid expansion in their application scope, from bio-mimetic dry adhesion [22], surface wetting control [23], and cell mechanics studies [24]. The newest addition to their list of application is air-flow transduction. Thanks to the excellent flexibility of PDMS, even tiny micropillars can bend substantially in response to air-flows such as wind and sound, leading to high sensitivity in acoustic sensing [25-27].

On top of that, elastomer-based soft-robots are gaining popularity as safe handlers of delicate objects [28-33]. Pneumatic actuation has been widely used for soft-robots thanks to its simplicity and efficiency [34, 35]. Applications like *in vivo* biomedical manipulation [36-39], however, require its microscale miniaturization, stimulating fabrication efforts to realize pneumatic micro-actuators [39-46].

Research Challenges

Despite such efforts, the realization of the unconventional elastomeric structures remains a great challenge, leaving only a small number of schemes available, especially, for producing 3D-networked, cylindrical MF channels, high aspect-ratio micropillars, and micro-scale soft-actuators.

For the realization of the MF channels that are both cylindrical and 3D-networked, a few fabrication schemes have been attempted. In the omni-directional printing scheme [47], cylindrical MF channels with 3D trajectories were fabricated by injecting cylindrical ink filaments that can be liquefied and drained upon solidifying the embedding material.

J. K. conceived the idea and supervised the research. J. L. and J. P. carried out the experiments and data analyses, together. J. K., J. L., and J. P. co-wrote the manuscript.

Fabrication schemes based on polymer molding of removable templates also achieved the goal with the utilization of 3D-shapable, cylindrical templates such as nylon [48], metal [49, 50], and polymer [51] wires. Self-assembly of micro-tubules [52] and direct UV-writing [53] have also been demonstrated recently. These existing fabrication schemes, however, are complicated and limited in their ability to realize essential 3D MF architectures such as 3D curved MF channels, internally looped MF channels which start and end within the embedding polymer block, and properly tapered MF channel junctions which enable physiologically realistic flow patterns for the vaso-mimetic LoCs' cell culture and hemodynamic modeling [7, 54, 55]. Schemes in which the template has to be physically pulled out require pre-swelling of the embedding polymer block, a process prone to deform the pattern [48, 49]. Moreover, such schemes cannot produce internally looped MF channels. Thermally dissolvable metal wires tend to produce channels with initial diameter > 300 μm [50]. Only recently was the channel size issue addressed by casting thermally dissolvable polymer into a very thin fiber form [51]. Most template based schemes are also very limited in their ability to form proper 3D MF junctions, in which the center of one cylindrical channel's cross section meets the side of the other channel at its *midline*. Forming such a junction needs end-to-side bonding of two cylindrical templates. With the template materials not providing effective bonding methods, end-to-side junctions have been made by thermal [48, 51] or mechanical [49] fusion of two simply overstacked templates. Such processes, however, hamper the formation of predictable junction shapes, let alone the tapered ones required for vaso-mimetic LoCs. Omni-directional printing, [47] self-assembly, [52] and UV-writing [53] schemes are more promising in these aspects but the accompanying demands for specialized instruments and materials prevent their wide adoption.

Reports of realizing high aspect-ratio PDMS micropillars with mm-scale heights, while keeping their diameters at μm-scale, have been also scarce so far, especially when it comes to upright ones capable of standing on their own [56-58]. This scarcity should be attributed first to the inherently low Young's modulus of PDMS (~1 MPa) [59]. Owing to the softness, the thin and long PDMS micropillars are prone to bend and collapse, often ending up with irreversible bonding to the substrate [60]. Existing fabrication techniques relying heavily on conventional, replica-molding also add difficulties by requiring de-molding process of the cured PDMS micropillars. Despite the efforts to improve the yield of the process, the failure rate inevitably increases with the height and aspect-ratio. For these reasons, the height and aspect-ratio of PDMS micropillars have been capped at ~700 μm and ~20 so far, respectively [56]. The resulting limitations in the achievable height and aspect-ratio of PDMS micropillars are particularly detrimental to their use as air-flow transducers because such geometric limitations in the PDMS micropillars lower the level of their deflection under air-flows, degrading the acoustic sensing sensitivity.

The pneumatic actuation is an already proven scheme in large-scale soft-robotics [32, 34, 35] but its microscale implementation entails many technical challenges [61, 62]. First, current soft-lithographic microfabrication techniques, developed mainly for building planar elastomer structures with low aspect-ratio patterns such as microchannels, are not ideal for constructing three-dimensional, hermetically sealed cavities required for pneumatic actuation. We can still build them by bonding two planar structures [40-43, 63] or employing dissolvable templates [64]. But the strength and yield of bonding decreases rapidly with the length-scale. Dissolving templates often becomes an equally complex task at microscale. Moreover, large-scale pneumatic actuators rely on many sub-elements, such as surface

corrugation or valves [61, 62], that are neither simple nor desirable to replicate exactly at microscale. In all, a successful microscale realization of a pneumatic soft-actuator requires a combination of new designs and fabrication techniques optimized specifically to that length-scale.

Dissertation Organization

As my dissertation work, I first demonstrate a new, unconventional fabrication scheme for 3D-networked, cylindrical MF channels, which addresses all issues stated above. The scheme allows facile realizations of highly curved 3D MF channel trajectories, proper MF junctions, and internally looped MF channels. The diameter of the MF channels can be well below 100 μm. It also allows the formation of tapered junctions and locally dented MF channels, which will especially benefit vaso-mimetic applications. Utilizing only water-based, low-temperature processes, the scheme is ideal for rapid prototyping of LoCs without fume-hoods or clean room facilities. Also, as potential applications of the MF channels for point-of-care monitoring, I report the implementation of the bokeh-effect-based microscopy scheme in microfluidic settings. For this work, I realize the integration using a single polymer microlens fabricated over a MF channel which was realized through my unconventional fabrication scheme for 3D-networked, cylindrical MF channels. The inherent simplicity of the bokeh microscopy enabled image capturing with an off-the-shelf camera.

Secondly, I will present another unconventional soft-lithography fabrication scheme which enables the realization of PDMS micropillars exceeding 2400 μm in height and 100 in aspect-ratio through the combined utilization of the direct drawing and the *in situ* heating. It also allows automatic integration of microspheres at the tips of the micropillars in a self-

aligned fashion. As a validation of the structure's utility for acoustic sensing, I demonstrate optically interrogated acoustic sensors based on the high aspect-ratio, microsphere tipped PDMS micropillars, in which the micropillar and microsphere functions as a flexible upright waveguide and a self-aligned reflector, respectively.

Lastly, I present one combination of new designs and fabrication techniques for realizing a microtube-type pneumatic soft-actuator that can be extended to micro-robotic tentacles. For this work, I establish a new bonding-free fabrication technique for long and thin, highly deformable microtubes and a semi-analytical model for their shape-engineering. Based on them, I amplify the microtube's pneumatic bending into multi-turn inward spiraling. The resulting micro-tentacle exhibit ~200 μm final radius of curvature and ~0.78 mN of grabbing force, rendering itself ideal for safe manipulation of soft, fragile micro-objects. This spiraling tentacle-based grabbing modality, the direct peeling-enabled elastomeric microtube fabrication technique, and the concept of microtube shape-engineering are all unprecedented and will enrich the field of soft-robotics.

The following chapters are organized based on four published journal papers of which I am the first/primary author.

CHAPTER 2

SUCROSE BASED FABRICATION OF 3D NETWORKED, CYLINDRICAL MICROFLUIDIC CHANNELS

Modified from a paper published in *Lab on a Chip*

Jiwon Lee, Jungwook Paek, and Jaeyoun Kim*

Abstract

I present a new fabrication scheme for 3D-networked, cylindrical microfluidic (MF) channels based on shaping, bonding, and assembly of sucrose fibers. It is a simple, cleanroom-free, and environment-friendly method ideal for rapid-prototyping of lab-on-a-chip devices. Despite its simplicity, it can realize complex 3D MF channel architectures such as cylindrical tapers, internal loops, end-to-side junctions, tapered junctions, and stenosis. The last two will be of special use for realizing vaso-mimetic MF structures. It also enables molding with polymers incompatible with high temperature processing.

Introduction

Microfluidic (MF) channels with rectangular cross-sections and 2D planar, trajectories, have been the workhorse of lab-on-a-chip devices. Recent expansion in the LoC's scope of application such as tissue scaffolding [7-9] and controlled hemodynamic studies [10-12], however, introduced an increasingly diverse set of requirements on the MF channel's cross-sectional shape and topology. Of special interest is the demand for 3D-networked, cylindrical MF channels originated from the efforts to mimic biological vasculatures. Existing fabrication schemes for such vaso-mimetic systems, however, have

---

J. K. conceived the idea and supervised the research. J. L. and J. P. carried out the experiments and data analyses, together. J. K., J. L., and J. P. co-wrote the manuscript.

been complicated and limited in their ability to realize physiologically realistic MF channels that are both cylindrical and 3D networked [48-53].

In this chapter, I demonstrate a new scheme which enables for the realization of MF channels with circular cross-sections and 3D trajectories, with an emphasis on realizing physiologically realistic MF channel architectures such as highly curved 3D MF channel trajectories, proper MF junctions, and internally looped MF channels. It also allows the formation of tapered junctions and locally dented MF channels, which will especially benefit vaso-mimetic applications. On top of that, the scheme utilizes only water based, low temperature process, which is ideal for rapid prototyping of LoCs without fume-hoods or clean room facilities.

The main enabling factor for the realization of 3D-networked, cylindrical MF channels is the use of sucrose as the template material. Sucrose is a readily available material that can be drawn into thin cylindrical fibers at low temperature. The resulting fibers exhibit mechanical and surface characteristics suitable for handling, shaping, and formation of transparent MF channels. Removal of the sucrose fiber requires only warm water, allowing fabrication of complex MF networks in fumehood-free settings. It also permits the use of polymers incompatible with strong etchants and/or high molding temperature. These beneficial features of sucrose as a sacrificial template material have been exploited for LoC fabrication in two different ways. Bellan *et al.* fabricated 3D artificial vascular structures by melt-spinning random sugar fiber networks and then molding them with curable polymer [65]. On the other hand, Li *et al.* fabricated bundles of poly-(L-lactic acid) (PLLA) tubules by coating sucrose fibers with PLLA and then dissolving the fibers, for eventual use as MF nerve scaffolds [66]. There has been, however, no explicit report on shaping/assembly of the

sucrose fibers to form 3D networks, as Esser-Kahn *et al.* have done with polylactide (PLA) fibers to make 3D vasculated structures [51]. Unlike sucrose, however, PLA template removal and fusion-based junction formation requires temperatures of 200–280 °C. Here, our scheme distinguishes itself from other sucrose-based methods by providing specific techniques to shape, assemble and bond the sucrose fibers. They allow us to build pre-designed, rather than random [65] or monotonically tubular [66], 3D networks of cylindrical MF channels, which will eventually lead to vaso-mimetic LoCs.

Fabrication of 3D-networked, Cylindrical Microfluidic Channels

Pulling and shaping of sucrose fiber templates

Steps for sucrose fiber fabrication are described in Fig. 1a–b. Sucrose (S5–500, Fisher) was melted at 200 °C for 10 min. Then we decreased the temperature to 125 °C and waited for 20 min at which the sucrose viscosity became optimal. While maintaining the temperature, we pulled sucrose fibers with a cylindrical rod moving at 0.1–26 cm s^{-1}. The pulling speed mainly controlled the sucrose fiber diameter. The diameter of the pulling rod was also important. For sucrose fibers with diameter <80 μm, we used a 125 μm-diameter glass fiber (SMF-28, Corning). For thicker ones, we used jacketed SMF-28 (900 μm in diameter). We routinely produced highly uniform fibers with less than ±5 μm deviation in diameter. The fibers were examined with optical (EZoom6, Edmund) and atomic force (Veeco) microscopes. We routinely obtained fibers with their diameters ranging from 30 to 900 μm. Diameter <30 μm led to handling difficulties. The upper limit was only set by the availability of adequate pulling rods and the ability to maintain a constant temperature over its facet. The fibers were then shaped in preparation for the assembly, as shown in Fig. 1c.

The sucrose fibers with diameter <50 μm are flexible enough to be shaped into diverse 3D forms at room temperature directly. In addition, by controlling the pulling conditions, we could taper the fibers as well.

Sucrose template bonding, assembly, and replication

Junctions were made by bonding one end of a sucrose fiber to the side of another. We used two methods, both based on the high water solubility of sucrose. In the first, we used steam to provide moisture and heat simultaneously. The two areas to be bonded were exposed to 90 °C water vapor for 3 s and then attached. Subsequently, the junction was annealed by a few seconds of extra vapor exposure. In the second method, we used sucrose mixed with 90 °C water at 2 : 3 weight-ratio as the adhesive as shown in Fig. 1d. The amount of required adhesive depends on the junction area. For instance, we applied 0.4 nL adhesive to bond 100 μm-diameter fibers. We added water continuously to maintain the adhesive composition. Whilst requiring an additional step, this method enables stronger bonding and a wider junction area. Furthermore, this method can produce tapered junctions, contributing critically to the vaso-mimetic effort. Therefore, through the aforementioned junction formation methods, the sucrose fibers were assembled into a 3D-networked template. Then, the completed template assembly (Fig. 1e) can be steam-annealed again to reduce surface roughness or residues. Then the sucrose template assembly was put into a container to be filled with the 10:1 mixture of PDMS base and hardener (Fig. 1f). Upon complete curing of PDMS, the sucrose fiber assembly was dissolved in water at 70°C and the channel was filled with red dye (Fig. 1g). Figure 1h shows one 3D MF network made within a PDMS cube.

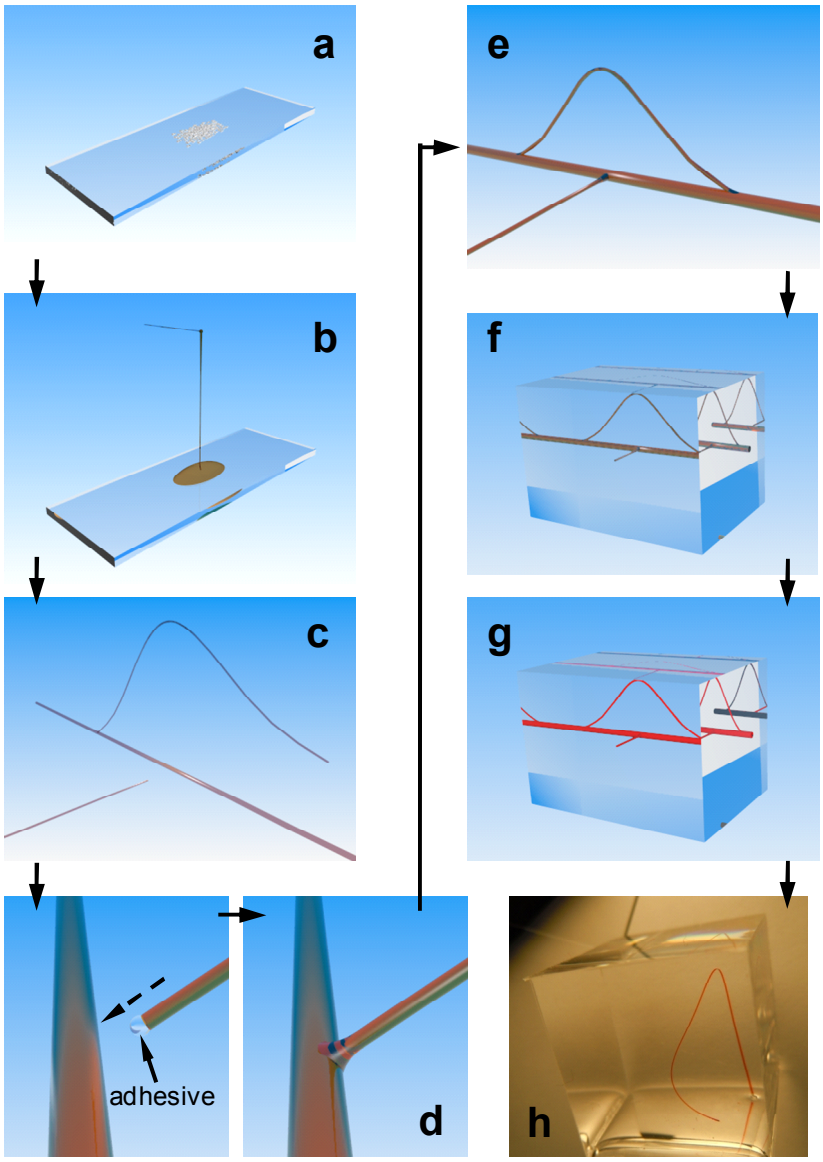

Fig. 1 Schematic outline of the sucrose-based rapid-prototyping process: (a) We melted sucrose and (b) pulled fibers which can be (c) shaped and (d) bonded with water-based adhesives (e) to form a template assembly. (f) Then we immersed it in liquid-phase PDMS. (g) Upon curing, the template was removed with water bath. For visualization, we filled the channels with dye. (h) A 3D MF channel in PDMS (scale bar: 5 mm).

Fabrication Results and Discussion

Physical characteristics of sucrose templates

Figures 2a to d show the microscope images of the sucrose fibers pulled at 2.0 ~ 25.6 mm/s in side and cross-sectional views. The graph in Fig. 2e also presents statistics obtained from five measurements. It indicates that thinner fibers pulled at higher speeds exhibit better repeatability in diameter, due probably to shorter exposure to environmental disturbances. The curve-fitting result shows that the diameter and pulling speed are related through an exponential decay function. Within the observed range of pulling speed, the sucrose templates exhibit excellent cross-section circularity.

Microfluidic junction formation

The water-dissolvable nature of sucrose facilitates the realization of MF channel junctions greatly. Two template bonding methods were described in the previous section. Figure 3a and b are the microscope images of two steam-bonded sucrose templates (633 and 220 μm thick) in side and top view, respectively. It is clear that the cross-sectional center of the thinner template meets the side of the thicker one at its midline, forming a proper end-to-side junction. The steam-bonding is also effective for attaching sucrose templates with greatly dissimilar diameters at a wide range of branching angle. Figure 3c shows a junction between sucrose templates with 594 and 63 μm diameters. Even though the two met at near-grazing angle, they formed a mechanically robust junction that can withstand subsequent manual handling. Fig. 3d shows the PDMS MF channel branch molded from the template in Fig. 3c. The flow of red dye clearly confirms proper MF channel branching. The branching point in Fig. 3d is actually located on the far side of the main channel and the transparency attests the excellent surface quality of the molded channel.

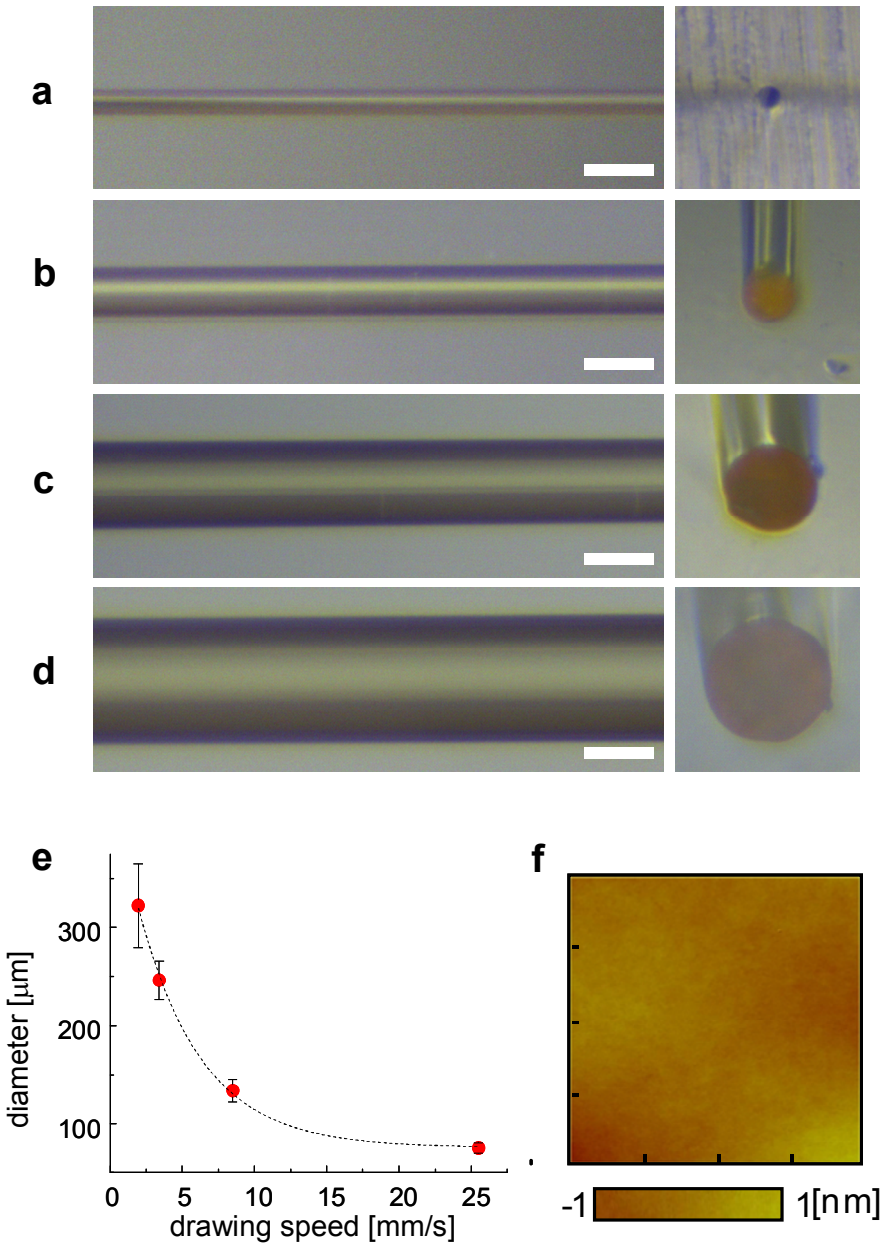

Fig. 2 Physical characteristics of sucrose templates: Optical microscope images of sucrose templates pulled at (a) 2.0, (b) 3.4, (c) 8.5, and (d) 25.6 mm/s in side and cross-section views. Scale bars: 100 μm. (e) The template diameter as a function of the pulling speed. The dotted curve represents an exponential decay. (f) An AFM scan image over a 4 × 4 μm^2 area on a sucrose template.

3D microfluidic channels trajectories and internal looping

The highly curved templates, such as the ones shown in Fig. 1e, can be bonded to other templates to realize more complex 3D MF networks. Thanks to the easy, water-based dissolution process for sucrose, the templates can take more complex forms such as internal loops. Figure 3e shows a template assembly with 3 internally looped, 68 μm-thick branches steam-bonded to a backbone. The backbone itself is tapered with its diameter changing from 622 to 237 μm over 2.5 cm (0.44° taper angle), achieving another important architecture in 3D. Figure 3e and its inset, a slightly rotated view, clearly show that none of the loops are in the same plane, forming a completely 3D network. The minimum radius of curvature was 1.43 mm. Figure 3f shows the flow of red dye through the multi-branching network molded from the template with PDMS, affirming the integrity of the MF network.

Vaso-mimetic architectures: tapered junctions and stenosis

Another important feature of this sucrose-based scheme is its ability to realize templates with their shapes varying rapidly in the axial direction. Figure 4a shows one example: a junction between two templates (387 and 61 μm in diameter) made with the second, adhesive-based bonding method. By controlling the volume of liquid adhesive and the speed of its application, a wide variety of junction shapes can be realized. Due to the total water-solubility of the adhesive itself, the PDMS-molded channels replicate the junction shape with high fidelity, as shown in Fig. 4b. As mentioned in Introduction, this tapered junction will contribute greatly to the realization of vaso-mimetic LoCs. As another example of axially modifying the template, we made a smooth dent (687 and 178 μm in length and height, respectively) to a 436 μm-thick sucrose template using the material's low temperature deformability. Figure 4c shows that the PDMS molded channel faithfully replicated the dent

shown in the inset. Such a localized deformation in a 3D-curved cylindrical microfluidic channel will function as an ideal testbed for studying the impact of stenosis on blood cells' hydrodynamic behaviors.

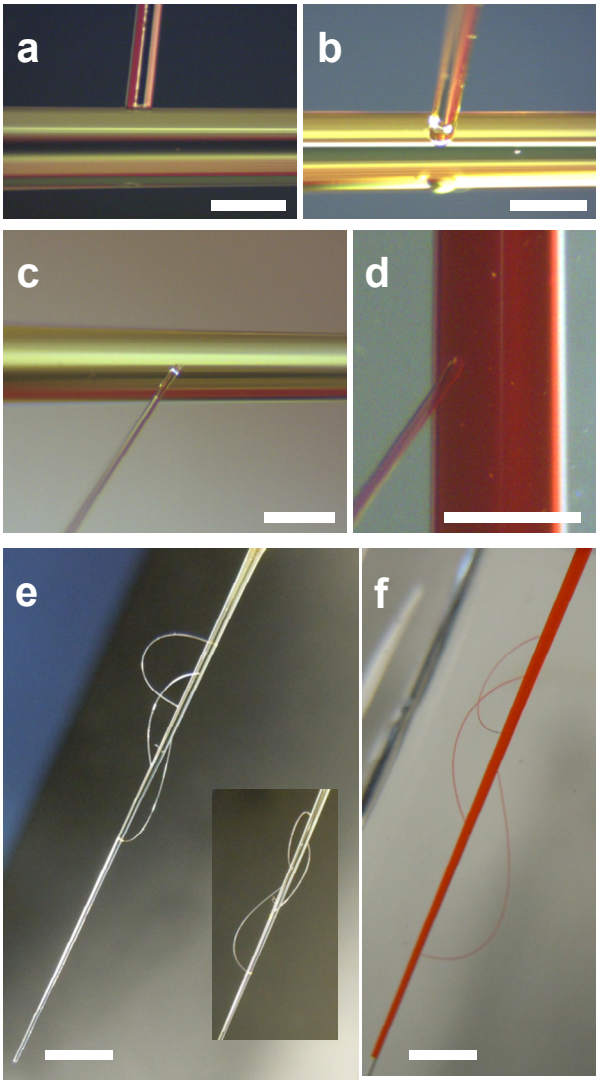

Fig. 3 Fabrication results of 3D MF channel architectures: An end-to-side junction formed between two sucrose templates in (a) side and (b) bird's eye view. (c) Steam-bonding is also effective between templates with greatly dissimilar diameters. (d) A MF channel branch PDMS-replicated from (c). The junction is located on the far side but clearly visible, confirming the transparency of the MF channel. (e) A 3D assembly of three internally looped templates to a cylindrically tapered backbone. No loop is in the same plane with another. (f) A 3D MF network made with (e). Scale bars: (a)-(d) 600 μm, (e)-(f) 5 mm.

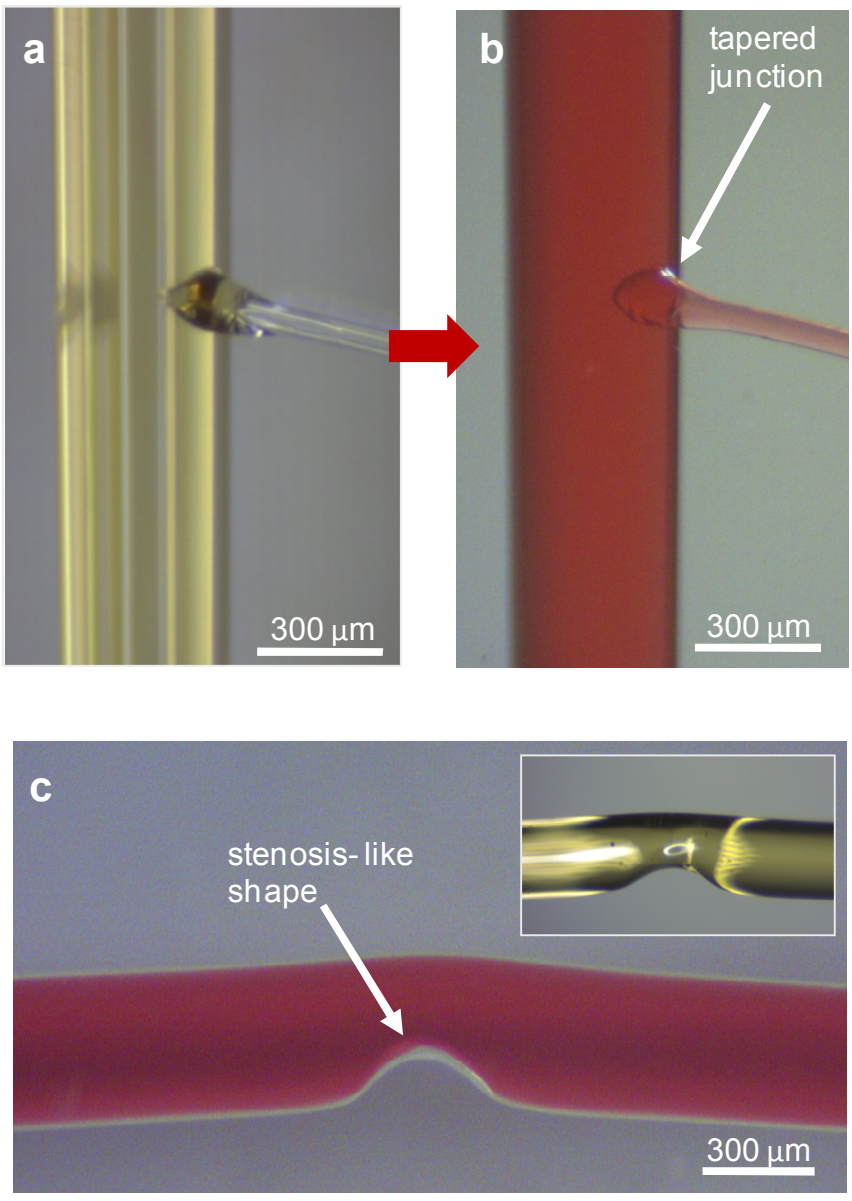

Fig. 4 Vaso-mimetic MF architectures: (a) A tapered junction between two sucrose templates bonded with water-based adhesive. (b) A PDMS MF channel molded from (a) with red dye flowing through the branch. (c) A stenosis-like structure formed by localized thermal deformation of the sucrose template (inset) and its PDMS molding. Scale bars: 300 μm.

Conclusion

In conclusion, I have demonstrated a simple and novel scheme to realize 3D-networked, cylindrical MF channels based on shaping, bonding, and assembly of sucrose fibers. It is a simple and fast method requiring no cleanroom facility or fume-hoods. Its total

reliance on sugar and water also makes the fabrication process highly environment-friendly. Despite its simplicity, our scheme can produce complex, pre-designed 3D networks, rather than the random or monotonic ones realized with existing schemes. The list of 3D MF channel architectures uniquely obtainable with our scheme includes: cylindrical tapers, internal looping, end-to-side junctions, tapered junctions, and local stenosis. The last two will especially benefit vaso-mimetic efforts, hemodynamic studies, and 3D tissue scaffolding. The low temperature required to dissolve the template will also allow molding with polymers incompatible with high processing temperature, such as PU.

Acknowledgements

This work was supported through National Science Foundation grants ECCS-1147413 and ECCS-0954845.

For this work, J. K. conceived the idea and supervised the research. J. L. and J. P. carried out the experiments and data analyses, together. J. K., J. L., and J. P. co-wrote the manuscript.

CHAPTER 3

BOKEH MICROSCOPE INTEGRATED MICROFLUIDIC CHANNELS FOR FACILE POINT-OF-CARE MONITORING

Modified from a paper published in *Biomedical Microdevices*

Jungwook Paek and Jaeyoun Kim*

Abstract

I report the implementation of the bokeh microscopy scheme in microfluidic settings for future applications in point-of-care microchannel monitoring in highly resource limited environments. I realize the functional integration using a single polymer microlens fabricated over the microchannel. The inherent simplicity of the bokeh microscopy enables image capturing with an off-the-shelf camera. Pilot devices exhibit 10~40 of magnification and 67~252 μm of field-of-view extent, confirming their utility for monitoring 50~100 μm microchannels carrying 10~50 μm objects.

Introduction

Successful realization of a point-of-care (PoC) diagnostic system not only requires accurate biosensors but also demands their efficient interface with the world outside [67]. Particularly for the recent thrust to extend the PoC service to very resource-limited environments, such as developing countries with little laboratory access, the interface needs to be highly simple and cost-effective as well [68]. One top priority task is the miniaturization and simplification of the light microscope, the primary conduit for optical signals and images [67, 69, 70]. Recent proliferations of smart cameras and phones are

helping the effort by making image-capturing and processing functionalities widely available even in the developing world, thereby letting the researchers focus only on the image formation [68, 71, 72].

Structurally, miniature microscopes reported so far deviate significantly from their prototypes. Most were cleverly simplified to allow the adoption of off-the-shelf components [73-75] or totally re-designed to exploit mass-produced, inexpensive optical devices such as webcams [76]. Their designs, however, still presume monitoring of a large sample area, which inevitably necessitates a wide field-of-view (FoV). With the PoC diagnostic systems rapidly increasing their reliance on MF channels, it would be rewarding to limit the FoV to a level just enough to cover a MF channel and exploit the resulting relaxation in the design constraints to further miniaturize and simplify the microscope [77]. To date, however, reports on such a trade-off have been scarce.

In this work, I exploit the trade-off to realize a simple mini-microscopy scheme specialized for PoC monitoring of MF channels. At the core of our scheme is the *bokeh* effect. In photography, it refers to the formation of bright circular disks by out-of-focus rays and has been exploited heavily to aesthetically blur images. Recently, MIT's Media Lab researchers utilized it for magnifying optical patterns [78]. There, one objective singlet converts the light from a small, illuminated pattern into angle-encoded ray-bundles, as shown in Fig. 5a. Collecting them with an ordinary camera with its lens range set to infinity enables magnified reconstruction of the original pattern. This scheme is misalignment-tolerant and depth-independent while requiring only a simple singlet on the object side. These beneficial features have rendered the scheme attractive not only for the originally intended application as a remotely resolvable optical tag, called *bokode*, but also for realizing simple, miniaturized

microscopes. Arpa *et al*. demonstrated a cell phone-based bokeh microscope using a tube-mounted lens let as the objective lens [79]. Here, I take one extra step by completely integrating the bokeh microscopy with microfluidic channels, equipping them with a built-in capability of microscopic monitoring.

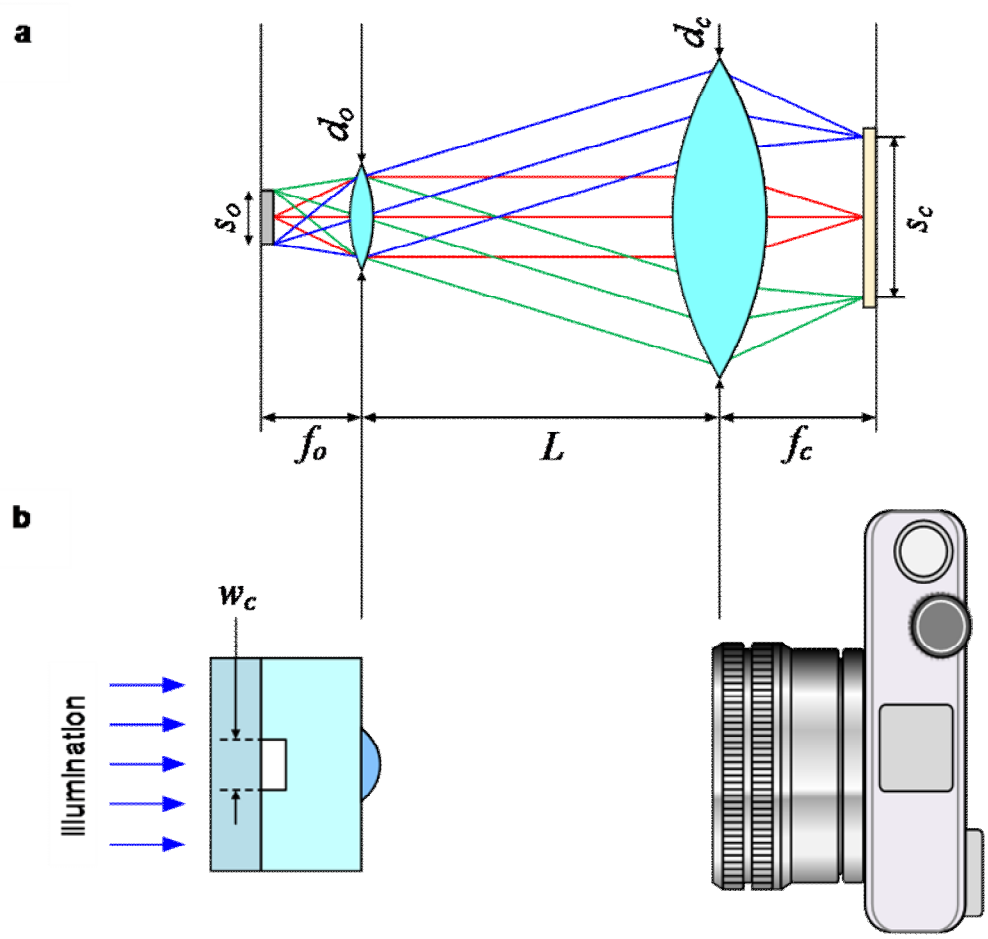

Fig. 5 Microfluidic channel integrated-bokeh microscopy scheme and its operation: (a) A schematic illustration of the operation principle of the bokeh microscopy. (b) A schematic diagram illustrating the integration of the bokeh microscope with a microfluidic channel. The polymer microlens functions as the objective lens. The camera, with its range set to infinity, takes the magnified image of the object.

Bokeh Microscope Design

Figure 5b outlines our scheme. The microfluidic device is fabricated with poly(dimethylsiloxane) (PDMS), a transparent elastomer. A microlens is integrated at the PDMS-air interface above the channel to function as the objective singlet. The depth of the channel is set to equal the focal length of the microlens. Below the MF channel is the illumination light source. The microlens first captures the light from the object in the MF channel and then converts it into angle-encoded ray-bundles. With a camera aiming at infinity, one can collect them and reconstruct a magnified image of the object.

Our design goal was imaging of objects at microbial length-scales (<50 μm) in typical MF channels (<100 μm) with an off-the-shelf camera. I began the design with the basic formulae given in Ref. [12] and refined it with LightTools™-based simulations. We chose Samsung NX100 as our imaging device for its immediate availability and low cost (<300 USD). With the range set to infinity, f_c of the camera lens can be varied from 20 to 50 mm. The corresponding f/#., *i.e.*, the ratio between f_c and the effective lens aperture d_c, are 3.5 and 5.6, respectively, setting d_c at 5.7 and 8.9 mm, respectively.

Since each sensor pixel is ~5×5 μm^2 in size, meaningful imaging of objects less than 50 μm in size requires a magnification $M = f_c / f_o$ exceeding 10. Monitoring of typical MF channels also requires the maximum object size $s_o = f_o \cdot d_c \cdot L^{-1}$ in excess of 100 μm. Since f_o affects M and s_o oppositely, a compromise is inevitable. In addition, one must also consider issues related to the fabrication and operation of the MF channel device. Microlenses with short f_o require a large surface curvature which is difficult to realize. On the other hand, long f_o translates into a wide microlens-channel separation, incurring misalignment and light absorption loss issues. Considering all these, we set 1.8 mm as our target f_o value. Table 1

summarizes the corresponding M and s_o for L=50 and 110 mm, which is very practical for the device-camera separation. Choosing a lens with longer f_c may lead to higher magnification and wider FoV but also reduce the amount of receivable light by limiting the f/#.

Table 1. Imaging characteristics of the camera lens at different f_c values and the corresponding magnification and FoV extent. All lengths are in mm. Experimentally measured values are given in parentheses.

f_c	f/#	d_c	$M = f_c / f_o$ f_o= 1.8	$s_o = f_o \cdot d_c \cdot L^{-1}$	
				L = 50	L = 110
20	3.5	5.7	11.1 (12.8~15.6)	0.205 (0.162)	0.093 (0.067)
50	5.6	8.9	27.8 (37.3~41.3)	0.320 (0.252)	0.146 (0.102)

Fabrication of MF Channel-Integrated *Bokeh* Microscope

With the basic design established as described above, we proceeded to fabricate the MF channel to be integrated with the bokeh microscope. For this work, we utilized our proprietary channel fabrication technique based on PDMS replication of water-soluble templates made of sucrose, the table sugar [80]. The process is described in Fig. 6. Since the templates were formed through direct drawing, they are inherently cylindrical. Consequently, the resulting microchannels exhibit circular, rather than more conventional square or rectangular, cross-sections. Such cylindrical MF channels are particularly beneficial for mimicking biological structures such as blood vessels. The sucrose templates used for this

work were approximately 70μm in diameter. As shown in Figs. 6a and b, we ensured that the microchannel is positioned precisely f_o below the PDMS/air interface by first placing the sucrose template on a pre-made PDMS slab with thickness f_o and then pouring and curing another batch of PDMS over them to form the lower half. We then fabricated the microlens at the PDMS/air interface by dispensing a droplet of UV-curable optical adhesive NOA-73 with a 400 μm-aperture micropipette actuated by a pico-pump (WPI, PV830) and curing it with UV light as depicted in Figs. 6c and d.

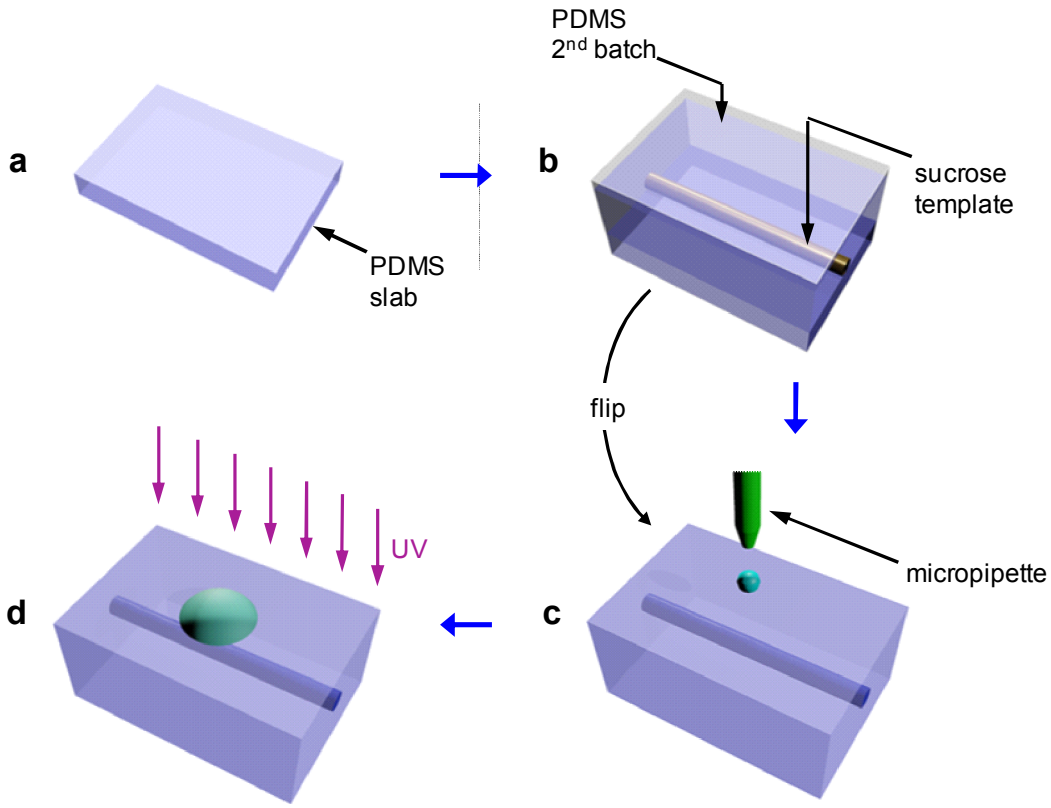

Fig. 6 Fabrication steps for a bokeh microscope-integrated microfluidic channel: (a) Preparation of a PDMS slab with its thickness matching f_o, (b) Placing of a cylindrical sucrose templatefollowed by pouring and curing of a 2nd batch of PDMS, (c) After dissolving the template, a UV-curable polymer droplet is dispensed on the air/PDMS slab interface and then (d) fixed by UV-illumination.

The most crucial part was aligning the microlens to the microchannel accurately so that the optical axis of the former passes through the center of the latter as shown in Fig. 7a. For that, we ran a laser beam through the tip of the micropipette and used it as the guiding beam. Then, we cured the NOA-73 droplet by illuminating UV light at 8 mW/cm^2 for 60 sec. Figure 3b shows an optical micrograph of a completed microlens. The optimal fabrication condition that would produce a microlens with its f_o precisely matching our target value of 1.8 mm was found iteratively. After each fabrication attempt, we extracted its profile from the image as shown in Fig. 7c and performed ray-tracing analysis with LightTools^{TM}. With the pneumatic pressure and pulse width set to10.0 psi and 200 ms, we could obtain a microlens with the right profile, as confirmed by the ray-tracing result plotted in Fig. 7d. The corresponding structural parameters *h, d_o,* and *r.o.c.* were 380 μm, 1450 μm, and 880 μm, respectively. The ~100 μm depth of focus was also adequate for imaging the microchannel fabricated above.

This "dispense-and-cure" scheme is better suited for microlens fabrication in resource-limited settings than those based on replica-molding which require complicated photolithography for master pattern generation and/or chemical or physical etchings for the pattern transfer. The laser-based microchannel-microlens alignment can also be done with readily available low-power laser pointers and constitutes another point of simplification in the sense that it eliminates the requirement for a microscope-base imaging for the alignment. Even though we did not use pre-made patterns to define the size of the droplet on the PDMS surface, the reproducibility was excellent. For example, from three trials of 880 μm-r.o.c. microlens fabrications, we obtained 877 μm in average with only 8.5 μm in standard deviation. Finding the optimum droplet volume which would result in the best matching with

the microfluidic channel had to be found through iterative fine tuning of the dispensing conditions due to subtle discrepancies between the idealized model and the experimental results.

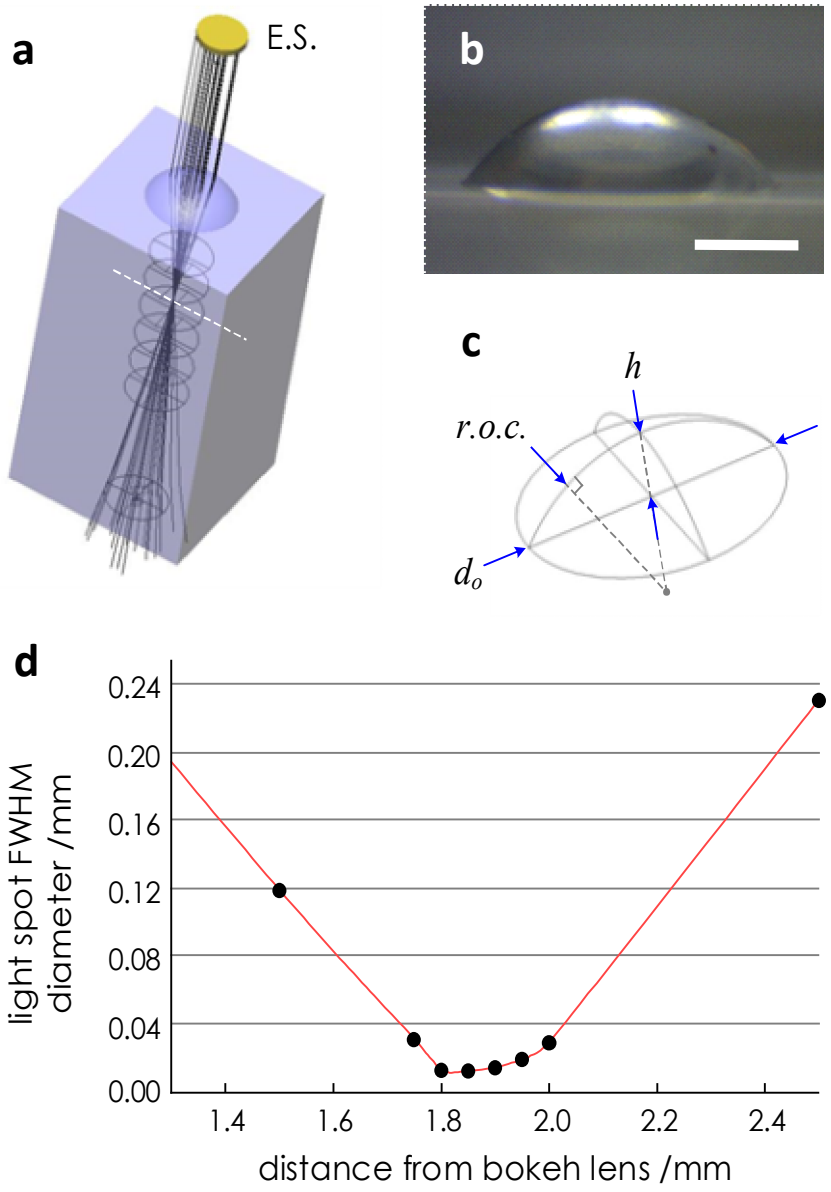

Fig. 7 Optical design of bokeh-effect-enabling microlens: (a) A snapshot of ray-tracing with the proper microchannel position marked as a white dotted line. E.S. stands for the extended source for the simulation. The circles indicate the positions of spot size evaluation. (b) Optical micrograph of the completed microlens (scale bar: 500μm) and (c) its model for ray-tracing. (d) At the iteratively obtained optimum condition, the microlens exhibits 1.8 mm focal length with ~100 μm depth-of-focus.

Characterization of *Bokeh* Microscope

We then tested the bokeh microscopy-based monitoring of the microchannel. The setup was simple as depicted in Fig. 5b schematically. The microchannel was illuminated from the backside with a light emitting diode (Thorlabs, MCWHL2) generating white light. We collimated the light and limited the beam diameter to 1 mm, which is ~2/3 of d_o, using an iris. Illumination over a wider area would generate rays reaching the camera without interacting with the object, and hence with no encoded information, and eventually degrade the bokeh image. The camera was positioned at a distance of 50~ 110 mm from the microlens using a tripod. As the camera's range was adjusted to infinity, the microchannel's image emerged from the circular light disk as shown in Fig. 8. We can control the FoV and magnification by varying L and f_c, as described previously. As the in-channel object to be monitored, we utilized translucent green microspheres (Cospheric, GPMS-0.98) made of polyethylene (n=1.503 at λo=555 nm). They were mono-dispersed with 36 μm in mean diameter with ±9 μm spread. We mixed them with glycerol (n=1.472 at λo=555 nm) and flew the mixture through the cylindrical microchannel fabricated above using a syringe pump.

Figures 8a to d show the imaging results for different combinations of the f_c and L values specified in Table 1. To estimate the magnification, we first counted the number of pixels corresponding to the whole extent of the microchannel. Using the known pixel size (~5×5 μm^2), we could calculate the channel width on the image sensor which, when divided by the known width of the microchannel, gives the magnification M. The FoV extent, or so, was also estimated by comparing the diameter of the circular light disk and the microchannel width. The results are given in Table 1 in parentheses. Comparison of the predicted and measured values reveals that M has been underestimated by a factor of ~0.75 while so

overestimated by ~1/0.75. We ascribe such systematic discrepancies to the differences in the values of f_c and d_c from their catalog values. The camera lens we used contains 9 lenses grouped into 8, which makes the estimation of its effective focal length and aperture very difficult. For the originally intended application of PoC microchannel monitoring in resource-limited settings, the performance of the bokeh microscope shouldn't be too sensitive to the choice of the camera or its lens. The obtained values of M and so, spanning 10~40 and 67 ~ 252 μm, respectively, are ideal for such PoC microchannel monitoring.

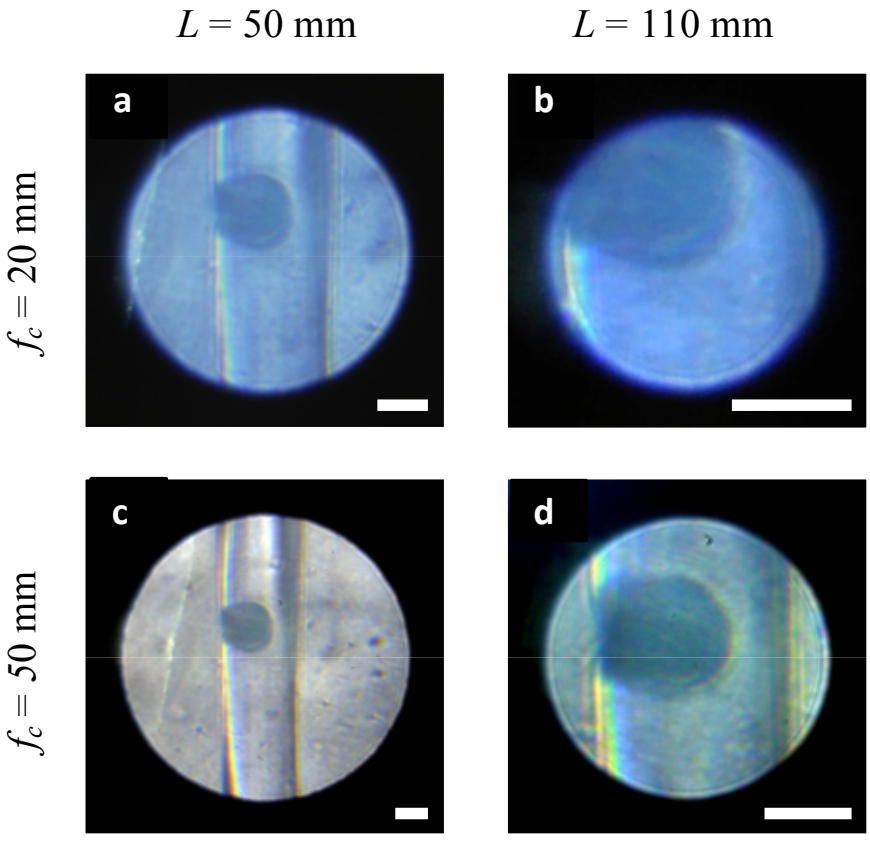

Fig. 8 *Bokeh* micrographs obtained with different combinations of f_c and L (scale bar = 30 μm for all)

Conclusion

As potential applications of the MF channels for PoC monitoring, I have successfully demonstrated the implementation of the bokeh microscopy integrated with the MF channels realized through our proprietary fabrication technique. Thanks to the inherent simplicity of the bokeh microscopy scheme, the integration required installation of a single microlens on the microfluidics side while allowing the microlens-generated image to be captured by an ordinary, widely available camera, which greatly facilitates its use for PoC applications in highly resource-limited settings. Developing new designs for the microchannel-coupled microlens and fabrication techniques for its realization constitutes the main body of the work. Analysis of the images of microchannel and its contents, obtained with an off-the-shelf camera, indicate that the simple scheme is capable of providing optical magnification and FoV extent in the range of 10~40 and 67~ 252 μm, respectively. With ~100 μm in depth-of-focus, the present bokeh microscopy scheme offers an ideal platform for facile monitoring <100 μm-wide microchannels carrying 10~50 μm objects. By achieving all these with a simple polymeric lens directly integrated with microfluidics, this scheme overcomes successfully compensate for its inherent limitation in imaging resolution and sensing versatility.

Acknowledgements

This work was supported through National Science Foundation grants ECCS-0954845.

For this work, J.K. conceived the idea and supervised the research. J.P. carried out the experiments and data analyses. J.K. and J.P. co-wrote the manuscript.

CHAPTER 4

MICROSPHERE-ASSISTED FABRICATION OF HIGH ASPECT RATIO ELASTOMERIC MICROPILLARS AND WAVEGUIDES CHANNELS

Modified from a paper published in *Nature Communications*

Jungwook Paek and Jaeyoun Kim*

Abstract

High aspect-ratio vertical structures have been intensely sought after in microtechnology but their realization has been a continuous challenge, especially when attempted with soft materials. Here, I present a direct drawing-based fabrication technique for upright PDMS micropillars. Despite the material's softness, the technique enables routine production of micropillars exceeding 2400 μm in height and 100 in aspect-ratio. It also supports self-aligned integration of microspheres at the micropillar tips, which greatly widens their application scope. To validate the utility of the microsphere-tipped micropillars, I configure them into air-flow sensors, in which the microspheres function as self-aligned mirrors, helping optical read-out of the micropillar's deformation. The micropillars' high aspect-ratio and the material's excellent flexibility greatly enhance their flow-induced deformation and enable mm/s-scale detection resolution. The results are highly supportive of the technical utility of the new structure which uniquely integrates high aspect-ratio PDMS micropillars and microspheres in a self-aligned fashion.

Introduction

Microscale PDMS pillars are rapidly expanding their application scope in small-scale technology [13-21] and the newest addition to their application list is mass-flow transduction [26]. Thanks to the excellent flexibility of PDMS, even a tiny micropillar can bend substantially in response to mass-flow, enabling highly sensitive transduction in a small form-factor.

The sensitivity of the micropillar-based mass-flow transducer depends critically on the micropillar's geometry. In general, those with higher aspect-ratios and millimeter-scale height, are preferred for their greater deformability. Realizing high aspect-ratio PDMS micropillars with millimeter-scale height, however, is very challenging, especially with the use of the conventional, replica-molding-based microfabrication techniques. The main obstacle is the need to de-mold the cured PDMS micropillars. Despite the efforts to facilitate the de-molding process [21], the failure rate increases inevitably with the height and aspect-ratio. The inherently low Young's modulus of PDMS (typically < 1 MPa) [59] is another source of difficulty since it frequently leads to the collapse of the PDMS micropillar and their irreversible bonding to the substrate [60]. Due to these reasons, the highest values for the micropillar height and aspect-ratio have been limited below ~400 μm and ~20, respectively, so far [56].

Here, I present a new soft-lithographic fabrication method, enabling the realization of high aspect-ratio PDMS micropillars. The key enabling factor is the adoption of the *direct drawing* technique. As shown in Fig. 9, it exploits rapid solidification of the capillary bridge, eliminating the need for de-molding. To date, the direct drawing technique has been applied to polystyrene [81], PMMA [82], PTT [83], nylon [84], sucrose [81], polyurethane [85], SU-

8 [86], and adhesives [87]. Its application to PDMS, however, has not been reported due mainly to the material's slow solidification rate and inherent softness. We address the issues by incorporating *in situ* heating into the drawing process so that the PDMS micropillar gets simultaneously hardened and solidified during its formation. The new technique enables routine production of upright PDMS micropillars that are up to 2.4 mm in height and over a 100 (~112) in aspect-ratio.

A more interesting feature of our technique is the use of microspheres as the drawing probes, as shown in Fig. 9b, which leads to the realization of *microsphere-tipped* micropillars (MSMPs). The integrated microspheres can play multiple roles. They can increase the micropillar's tip-visibility, facilitating microscope-based metering of their bending levels [56]. They can also function as the tip-mass which tunes the MSMP's motion dynamics. The variety in the size and composition of commercial microspheres further widens the MSMP's application potential.

To validate the utility of the microsphere-tipped PDMS micropillar, we turn it into an optical air-flow sensor for which both the aspect-ratio and microsphere-tipped architecture play enabling roles. High aspect-ratio PDMS micropillars naturally suit the task of air-flow sensing. The outstanding flexibility of the material and the μm-scale diameter allow substantial flow-induced bending even in very short micropillars that can barely stand out above the stagnant boundary layer. A full exploitation of the merit, however, requires an effective read-out scheme that can accurately report the micropillar's bending level with ease. For this, we utilize the microsphere to implement the optical read-out scheme outlined in Fig. 9f. There, the PDMS micropillar functions as a flexible waveguide. The probe light enters the micropillar from the base and then gets reflected at the top facet back into the

photodetector. The flow-induced bending of the micropillar reduces the reflection power through spoiled waveguiding and beam deflection.

Critical to the success of the scheme is guaranteeing high-level reflection at the micropillar's top facet. We accomplish it by capping the micropillar with a Ag-coated microsphere and used its surface as the reflector. Manual installation of microspheres can be tedious and error-prone [56]. In contrast, our microspheres are installed automatically in a *self-aligned* fashion. Overall, both the fabrication technique itself and the resulting structure, which uniquely combines high aspect-ratio micropillars and self-aligned microspheres, turn out to be capable of expanding the scope of soft material-based microtechnology.

Fabrication of Microsphere-Tipped PDMS Micropillars

We started out with the preparation of the drawing probe array (Fig. 9a). The microspheres were first assembled on a photo-lithographically patterned SU-8 grid and then transferred onto a piece of double-stick tape attached to a glass substrate. We used two types of microspheres as the drawing probes: ~50 μm-diameter PMMA microspheres and ~58 μm-diameter Ag-coated hollow glass microspheres. The latter was more effective for increasing the levels of reflection and tip-visibility. We then flipped the array and attached it to a micro-manipulator (Fig. 9b). We also spin-coated a thin (~25 μm) layer of PDMS and pre-baked it on a hot plate placed under the micro-manipulator. During the pre-bake, we lowered the microsphere array towards the PDMS thin film until the separation was reduced to 50 μm. Upon completion of the pre-bake, we further lowered the microsphere array so that it can physically contact and get immersed in the PDMS thin film (Fig. 9c). After 40 seconds of contact, we lifted the micro-manipulator at 144 μm s^{-1}, drawing PDMS micropillars (Fig. 9d).

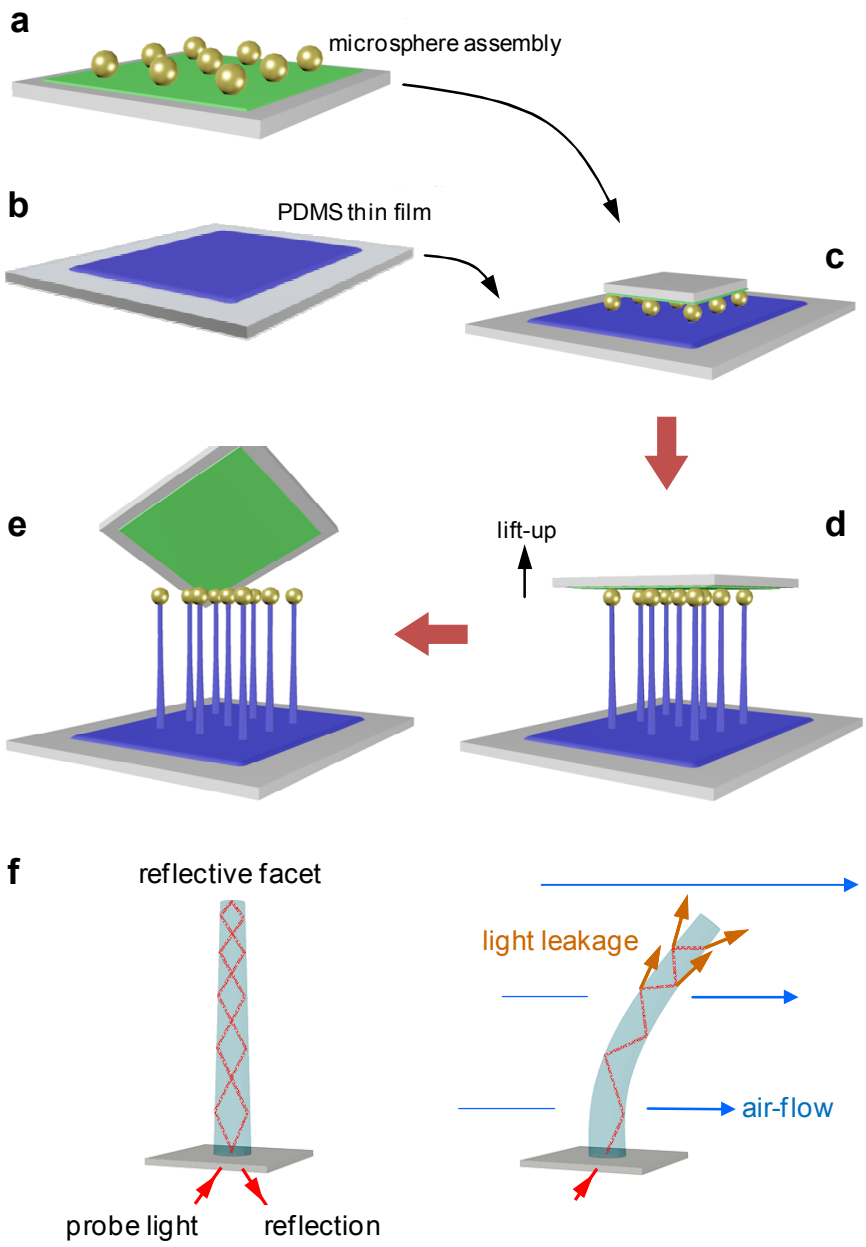

Fig. 9 Fabrication of microsphere-tipped PDMS micropillars and their optical air-flow sensing application: (a) Arraying of microsphere drawing probes on a piece of double-stick tape. (b) Spin-coating and pre-bake of a PDMS thin film. (c) Flip-contacting the microsphere array onto the PDMS thin film. (d) Micro-manipulator-assisted drawing of PDMS micropillars with *in situ* heating. (e) Removal of the double-stick tape upon the completion of the drawing process and post-bake. (f) The operation principle of the micropillar-based, optical air-flow sensing. In the absence of an air-flow, the micropillar stands upright, maximally reflecting the probe light. Under air-flows, the micropillar bends, resulting in a reduction in the reflection level.

The temperature was maintained at 100 °C throughout these steps for simultaneous solidification and hardening of the PDMS micropillars. Completed micropillars were then post-baked at 100 °C for 2 hours and at room-temperature for 24 hours. Finally, we detached the double-stick tape from the MSMPs (Fig. 9e). For this, we first moved up the micro-manipulator holding the double-stick tape so that the MSMPs got elongated by 100%. The resulting tension induces gradual detachments of the microspheres from the tape. It could take several minutes. At this step, the main cause of failure is insufficient curing of the PDMS micropillar which detaches the microsphere from the micropillar, rather than from the tape.

Fabrication Results and Impact of the *In Situ* Heating

Physical characteristics of PDMS micropillars

The direct drawing technique enabled routine fabrications of mm-scale PDMS micropillars with aspect-ratios >40. Here, we defined the aspect-ratio as the ratio between h, the distance between the substrate and the micropillar-microsphere interface, and d_{ave}, the average of the top, middle, and base diameters. The micropillar in Fig. 10a was drawn with a 50 μm-diameter PMMA microsphere. With its h and d_{ave} at 1134 and 13.5 μm, respectively, the micropillar exhibits an aspect-ratio of 84. Such a high aspect-ratio was attainable for arrayed micropillars as well. The micropillars in the 4×4 array shown in Fig. 10b were drawn with a matching array of 58 μm-diameter Ag-coated hollow glass microspheres. In average, they were 877.2 μm high and tapered with their diameter changing from 14.4 μm right underneath the microsphere to 29.8 μm at the base. With 20.8 μm in d_{ave}, their average aspect-ratio was 42. As pointed out above, capping the tip with a metallic microsphere

greatly enhanced the micropillar's tip-visibility. Figure 10c shows the highest micropillar obtained so far. With its h and d_{ave} at 2400 and 21.3 μm, respectively, the aspect-ratio reached 112. To the best of our knowledge, this is the highest aspect-ratio reported for a vertical PDMS micropillar.

Figure 10d shows the relation between h and d_{ave} of our micropillars. Initially, the aspect-ratio increases with h. Beyond $h \sim 1.1$ mm, however, the increase in h induces a matching increase in the base diameter, saturating the aspect-ratio in the range of 70~110. Among the micropillars, we chose the three in Table 2 as our model components for further characterization and air-flow sensing application.

Table 2. Characteristics of the PDMS micropillars under test : This table summarizes the structural characteristics of the three PDMS micropillars employed for the Young's modulus measurement and air-flow/sound sensing. f_o denotes the measured resonance frequency.

	h [μm]	d_{ave} [μm]	Aspect Ratio	f_0 [Hz]
A	800	19.8	40.4	
B	1600	22	72.7	102
C	2000	23	86.9	93

The simplicity of the MSMP fabrication process also renders it very robust. It took more than 140 pilot fabrications to optimize the process parameters such as the initial PDMS layer thickness, *in situ* curing temperature, and drawing speed. Once they were optimized, we have experienced few failures when fabricating MSMPs one by one. Most failures occurred during the fabrication of MSMPs in an arrayed format. In both cases, the MSMP's height and

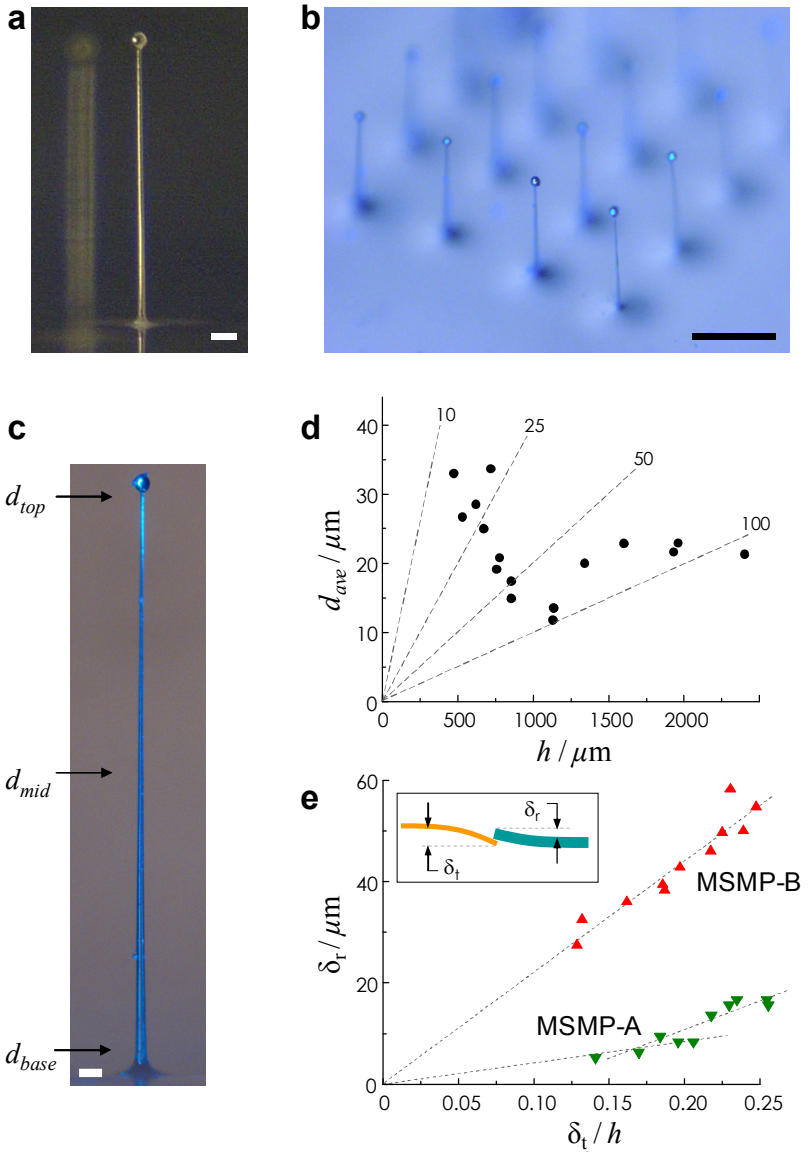

Fig. 10 Physical characteristics of the fabricated microsphere-tipped PDMS micropillars: Optical micrographs of (a) a 1134 μm-high PDMS micropillar integrated with a 50 μm PMMA microsphere. Its aspect-ratio is 84. (Scale bar: 100 μm), (b) a 4×4 array comprising 877.2 μm-high micropillars integrated with 58 μm Ag-coated hollow glass microspheres. (Scale bar: 700 μm), and (c) the micropillar with the highest aspect-ratio of 112 (d_{top} = 9 μm, d_{mid} = 14 μm, d_{base} = 41 μm, and h = 2.4 mm, scale bar: 100 μm). (d) The average diameter d_{ave} of the micropillar plotted as a function of h. The dotted lines mark the aspect-ratios. The data indicate that the aspect-ratio initially increases with h but stabilizes in the range of 70~110 once h exceeds ~1 mm. (e) The results of the reference-cantilever method-based measurements. The inset outlines the setup. The deflection length of the test cantilever (δ_t) induced by the reference cantilever with known mechanical properties was measured for different deflection levels (δ_r). The dotted lines represent the results of linear fit with zero or non-zero x-intersection assumed.

diameter exhibited finite spreads. The height of the MSMP could be controlled with μm-scale accuracy with the help of the micro-manipulator. The diameter, however, exhibited much wider spread. Our analysis revealed that both the spread in the diameter and the higher failure rate during arrayed fabrication arise from a common cause: the uncertainty in the depth of the microsphere's immersion into the semi-cured PDMS film right before the drawing (Fig. 9c). Shallower (deeper) immersion inevitably decreases (increases) the contact area between the microsphere and the PDMS film, leading to thinner (thicker) MSMPs. Insufficient diameter leads to collapse of the micropillar. Micropillars that are too thick, on the other hand, are more likely to fail during the detachment from the tape which requires ~100% elongation. The immersion depth depends on a number of factors including the degree of PDMS curing, the size of the microsphere, and the micro-manipulator's contact force. In the case of arrayed fabrication, the tilting of the microsphere assembly is added as the dominant factor.

The impacts of the immersion depth and contact area on the MSMP's diameter accuracy and failure rate were clarified through the study of the 4×4 MSMP array in Fig. 10b. Among the 16 MSMPs, one failed due to excessive thickness during the detachment step. As shown in Table 3, the standard deviation in the height was only 10.35 μm for an average height of 877.2 μm. On the other hand, the standard deviation in the diameter was much greater: 5.25 μm for an average diameter of 20.8 μm. Tables 4, 5, and 6 show the maps of the MSMPs' height, diameter, and the diameter of the microsphere, respectively. The height map in Table 4 clearly shows that the microsphere array/double-stick tape composite (Fig. 9d) was slightly tilted, mainly along the row direction of the Table, causing ~±15 μm deviations in the vertical positions of the microspheres and, hence, their immersion depths. The

corresponding change in the MSMP's diameter can be found in Table 5. The commercial Ag-coated hollow glass microspheres we employed for this work came with a 53~63 μm diameter range and the variations are listed in Table 6. Its correlation with the MSMP diameter, however, is weaker than that of tilting. The fact that the only failure occurred to the corner MSMP, which suffers maximally from the tilt in both row and column directions, re-assures the importance of leveling the microsphere array before drawing.

Table 3: Overall statistics of the height and diameter for the 4 x4 MSMP array shown in Fig. 10b

average height	standard deviation	average diameter	standard deviation
877.2 μm	10.35 μm	20.8 μm	5.25 μm

Table 4: Height map of the 4×4 MSMP array (all entries in μm)

892.7	885.4	869.8	failure
889.6	879.2	869.8	858.3
892.7	872.9	874.0	865.6
885.4	881.3	869.9	871.9

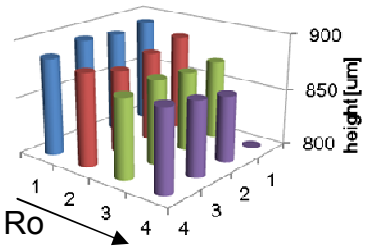

Table 5: Diameter map of the 4×4 MSMP array (all entries in μm)

11.8	22.6	25.0	N/A
12.2	21.2	25.3	25.3
14.2	23.6	25.0	22.6
13.3	21.9	22.6	26.7

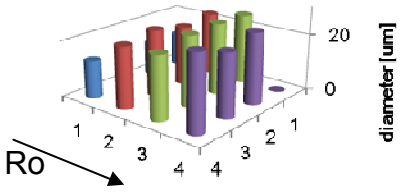

Table 6: Diameters of the microspheres used for the MSMP array fabrication (all entries in μm)

56.0	63.8	62.5	N/A
56.1	56.3	63.1	57.3
55.2	58.7	58.3	58.2
60.4	62.5	57.3	61.8

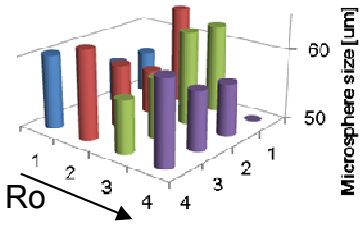

On the other hand, the minimum possible distance between two neighboring MSMPs, which determines the attainable array density, is mainly limited by factors arising from the adoption of the direct drawing-based fabrication technique itself. As shown in Fig. 11a, at the early stage of drawing, significant axiconic pedestals are formed around the micropillars. When two micropillars were within the pedestal radius of each other, they would exhibit a strong tendency of merging. The optical micrograph in Fig. 11b clearly shows the pedestals. For micropillars drawn with 53~63 μm-diameter microspheres, the pedestal diameter was d_p = 273.4±12.85 μm (std). In accordance, we could draw micropillars with interval greater than d_p with relatively high yield, as shown in the optical micrograph in Fig. 11c. As shown in the micrographs in Fig. 11d and e, however, micropillar pairs with intervals < d_p ended up failures with high probability. Therefore, we came to see that our direct drawing-based fabrication technique itself imposes certain limitations on the minimum possible distance between two neighboring micropillars.

In addition to the dimensions, the optical loss of the MSMP is also important for their future utilizations as flexible optical waveguides. Optical loss of various waveguide materials, both organic and inorganic, and the corresponding waveguide propagation loss have been intensively investigated so far [88, 89]. With ~20 μm in diameter and air-cladding,

the MSMPs can support a large number of higher-order modes, making the surface roughness, rather than the material absorption, the main cause of the optical loss. It is difficult to directly measure the propagation loss of optical waveguides < 3 mm in length. Previously, however, we have characterized lost wax-molded PDMS optical waveguides with cm-scale lengths and 100~200 μm diameters [17]. The AFM-measured surface roughness was in the range of 3.2±0.8 nm and the corresponding waveguide propagation loss was < ~3.5 dB cm^{-1}. For our current MSMPs, fabricated with no physical contact with molding structures, it will be reasonable to assume equal or lower surface roughness and propagation loss, which will be acceptable for their mm-scale operation lengths.

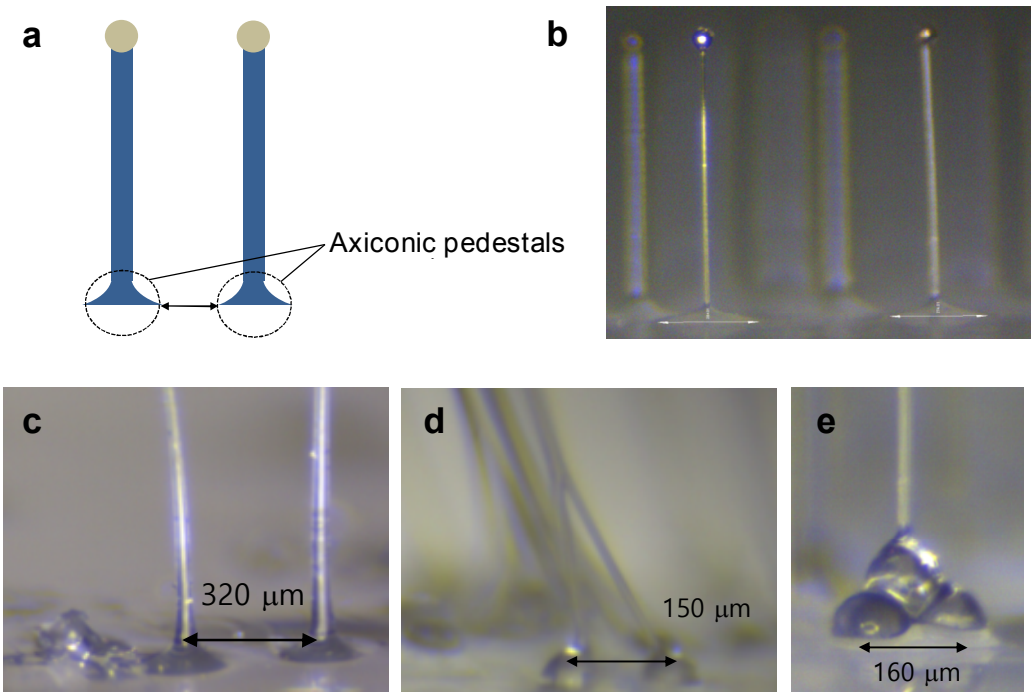

Fig 11 Micropillar merging as the limiting factor to dense array formation: (a) Directly drawn PDMS micropillar's axiconic pedestal and (b) its optical micrograph. Micrographs comparing separated (c) and merged (d,e) micropillars.

Impact of *in situ* thermal hardening

Given the observations that the directly drawn PDMS micropillars can stand upright and support the weight of microspheres despite their thinness and high aspect-ratio, we conjectured that the *in situ* thermal hardening has hardened PDMS to a certain degree and tried to quantify its impact by measuring the micropillar's Young's modulus E_Y. Among many available methods [90, 91], we adopted the *reference-cantilever method*, shown in the inset of Fig. 10e, in which a reference cantilever with known spring constant K_r is used to deflect the test cantilever and its spring constant K_t is estimated from the relation $K_t \cdot \delta_t = K_r \cdot \delta_r$ where δ_t and δ_r represent the deflection lengths of the test and reference cantilevers, respectively. For conically tapered beams, K and E_Y are related by $K = 3\pi \cdot E_Y \cdot d^4 \cdot T/(64 \cdot h^3)$ where T is the taper constant defined as d_{min} / d_{max} [92].

The three MSMPs in Table 2 were targeted for this characterization. The thin and long geometry of the PDMS micropillars and their material characteristics, which remains soft in absolute sense even after the thermal hardening, made it difficult to find adequate reference cantilevers. In our work, we chose a section of commercial PMMA fiber as the reference cantilever. Because the reported E_Y of PMMA vary widely, we determined the E_Y of our PMMA fiber by applying the reference-cantilever method to it using a section of communication-grade optical fiber as the reference cantilever. Since the optical fiber is made of highly pure fused silica, we could use the tabulated E_Y of fused silica to calculate K_r, K_t, and eventually the E_Y of the PMMA. The obtained $E_{Y,PMMA} = 3.0 \pm 0.18$ GPa which is close to the previously reported value (2.8 GPa) for the PMMA fiber from the same manufacturer [93].

We then applied the same method to the MSMPs using the PMMA fiber as the reference cantilever. For the first two MSMPs in Table 2 (*i.e.*, A and B), we could perform stable and consistent measurements of δ_r and δ_t while maintaining the δ_t values below 25% of the MSMP height which, according to the rigorous large deflection beam theory [94, 95], leads to a linear relation between the applied force and the cantilever deflection. MSMP-C, the longest one, however, was too flexible to be kept within the regime of $\delta_t/h < 25\%$ and excluded from the characterization. The measured δ_r–δ_t combinations are shown in Fig. 10e. In the case of MSMP-A, the δ_r–δ_t curve became nonlinear once δ_r exceeded 150 μm even though it is only ~20% of h, well within the linear regime. The corresponding increase in the δ_r/δ_t slope and E_Y may be the outcome of strain hardening which, according to a recent study, becomes severer with decreasing structure dimensions [96]. So, we extracted the δ_r/δ_t slope only from the linear, small-deflection regime and estimated E_Y based on it. For MSMP-A, the slope was ~0.0526. With d_{ave} and h of the un-tapered reference cantilever at 21 and 2600 μm, respectively, and those for the tapered (T = 0.45) MSMP-A at 19.8 and 800 μm, respectively, the estimated E_Y of MSMP-A was approximately 2.45 MPa which is higher than most E_Y values reported for bulk PDMS (~1 MPa) [59]. Obtaining such a high E_Y value in bulk PDMS requires hours of high temperature curing [97]. Beyond the point, the slope jumped to ~0.1414, suggesting even higher E_Y. In the case of MSMP-B, we had to use an even thinner and longer PMMA fiber section (d = 15.4 μm, h = 3517 μm) as the reference cantilever. The resultant δ_t/δ_r slope, shown in Fig. 10e, was constant around ~0.138. The corresponding E_Y was ~2.31 MPa which is very close to the MSMP-A estimate and still higher than typical bulk E_Y values. We attribute the ~1 MPa increase in E_Y to the *in situ* thermal hardening incorporated into the direct drawing process.

Air-Flow Sensing with Microsphere-Tipped PDMS Micropillars and Discussion

Sensing of steady state (non-time varying) air-flows

We then transformed the MSMPs in Table 2 into air-flow sensors by adding the optical read-out setup shown in Fig. 12a. Figures 12b to e show MSMP-A's deformation in response to air-flows with their velocities at 0, 0.12, 0.16, and 0.2 m s^{-1}, respectively. In the absence of an air-flow, as shown in Fig. 12b, the micropillar stands straight, producing maximal reflection. Upon contact with an air-flow, it bends due to the fluidic drag force, resulting in a decrease in its reflection level. Here, we further investigated optical mechanisms for the decrease. For this work, we set up a numerical model of the MSMP and the supporting optical setup and performed ray-tracing-based simulations. The numerical model of the MSMP structure, shown in Fig. 13a, was obtained first by extracting the curvatures of the MSMPs under air-flows from their microscope images and then adding volumes around them using known values of their diameters. A reflective sphere was added at each tip of the MSMPs to mimic the Ag-coated sphere in the real setup. For estimation of the light reflection, we exported the model into LightTools™ and performed ray-tracing as shown in Fig. 13b. We used a collimated, coherent light at 632.8 nm to model the probe light and applied material characteristics to each part of the setup.

The results of the ray-tracing-based simulations revealed that the decrease of the reflection level in the MSMPs undergoing flow-induced bending can be attributed to both the spoiling of the waveguiding and the deflection of the reflected light. From the comparison of the sum of the leakage power and the overall decrease in the reflection, the relative contribution of the waveguide spoiling to the reduction in the reflection was estimated to be ~10% even in the case of maximal MSMP bending, putting the deflection of the reflected

light as the dominant factor. Figure 14a shows the result of the simulation performed with the numerical model for MSMP-A of Table 2 (800 μm in height).

While the computed reflectance values exhibit deviations from the measured values in Fig. 15, the characteristic sigmoidal curve shape was successfully recovered through the simulation. It is interesting to point out that such a sigmoidal decrease in the light throughput is a signature feature of "eclipsing" of a Gaussian-like beam by an aperture. A recent example can be found in Ref. [18].

A more important feature presented in Fig. 14a is the dependence of the response curve on the size of the detector. More specifically, the size of the iris in front of the detector controls the response. Narrowing the iris will expedite the blocking of the reflected light from the detector and, hence, amplify the impact of light deflection. Through this, we can reduce the detection threshold value and enhance the slope and, hence, the sensitivity. We experimentally verified this simulation-based prediction. Since the iris opening was difficult to control with high accuracy, we fixed the opening diameter and varied the distance between the MSMP and the iris/detector complex. The results obtained with the 0.8 mm-high MSMP-A are shown in Fig. 14b. The impact of the narrowed iris opening, and hence the reduction in the detector size, was very pronounced both in the viewpoints of detection threshold and slope. This type of improvement in detection performance, which relies primarily on the reduction in the detector size, cannot be always encouraged since the attainable optical signal power has to be traded-off for its realization.

From numerical simulations, we found that the decrease can be ascribed to two mechanisms, *i.e.*, the spoiling of waveguiding and the deflection of the reflected light. And the corresponding changes in the reflection levels are plotted in Fig. 15 for all three MSMPs.

They commonly exhibit a quasi-linear regime sandwiched between two slowly-varying curved regimes. The onset of the first curved regime can be defined as the threshold velocity of the MSMP-based air-flow sensors. Figure 15 indicates that they were 0.07, 0.05, and 0.04 m s^{-1} for MSMP A, B, and C, respectively. The curves also indicate that the decrease in the reflection saturates beyond a certain velocity, forming a flat pedestal at 26~32% level. It is due mainly to the residual reflection at the air-glass interface, which is not affected by the air-flow, and can be reduced with anti-reflection coating. In the quasi-linear regime, the optically retrieved reflection level can function as a good measure of the air-flow velocity. The data represent 10-measurement averages. For all three micropillars, the fluctuation in the measured reflection level was maximal near the midpoints of the quasi-linear regimes with the standard deviations at 0.0215, 0.0208, and 0.0152 for MSMP A, B, and C, respectively. The error bars represent the standard deviation which is 0.2~3.8% of the mean values (1.67% in average). The slopes of the quasi-linear responses were -11.3, -17.8, and -27.7 s m^{-1} for MSMP A, B, and C, respectively. In conjunction with the standard deviations obtained above, these slopes set the limits of detection at 1.82, 1.16, and 0.55 mm/s for MSMP A, B, and C, respectively, for steady state, non-time-varying, air-flows.

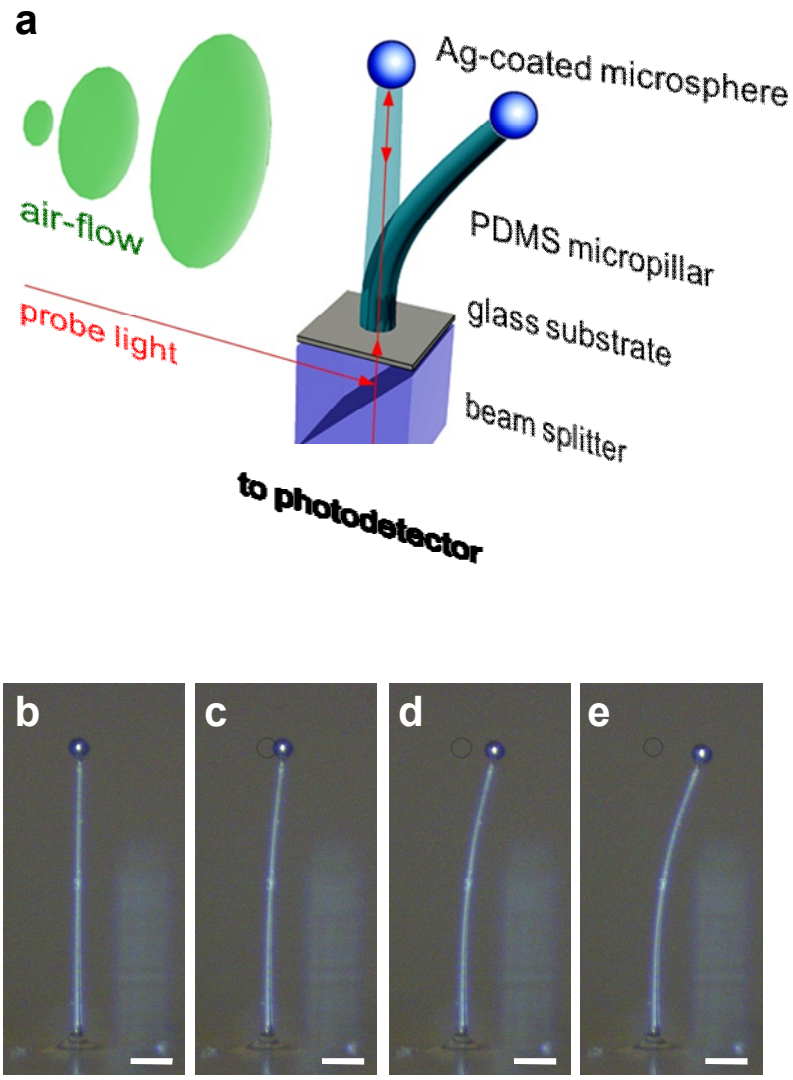

Fig. 12 Air-flow sensing with microsphere-tipped, high aspect-ratio PDMS micropillars: (a) The optical read-out setup for MSMP-based air-flow sensing. The three micropillars in Table 2 were utilized. The surface of the Ag-coated microsphere functions as the reflective top facet of Figure 9f. Micrographs in (b) to (e) show the gradual increase in MSMP-A's bending as the air-flow velocity increases from 0 to 0.12, 0.16, and 0.20 m s^{-1}, respectively. (Scale bars: 100 μm)

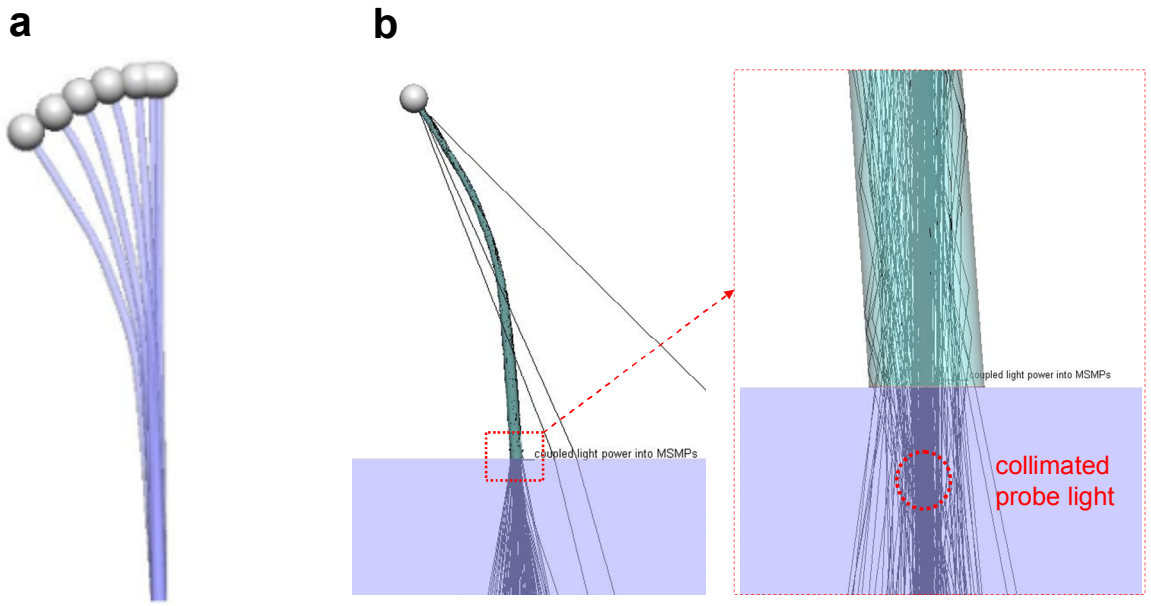

Fig. 13 Optical investigation for a decrease in a bent MSMP's reflection: (a) CAD models for ray-tracing-based simulations of bent MSMP structures (b) A snapshot of the ray-tracing showing the in-coupling of the collimated probe light, reflection, and light leakage due to MSMP bending, and out-coupling of the reflection.

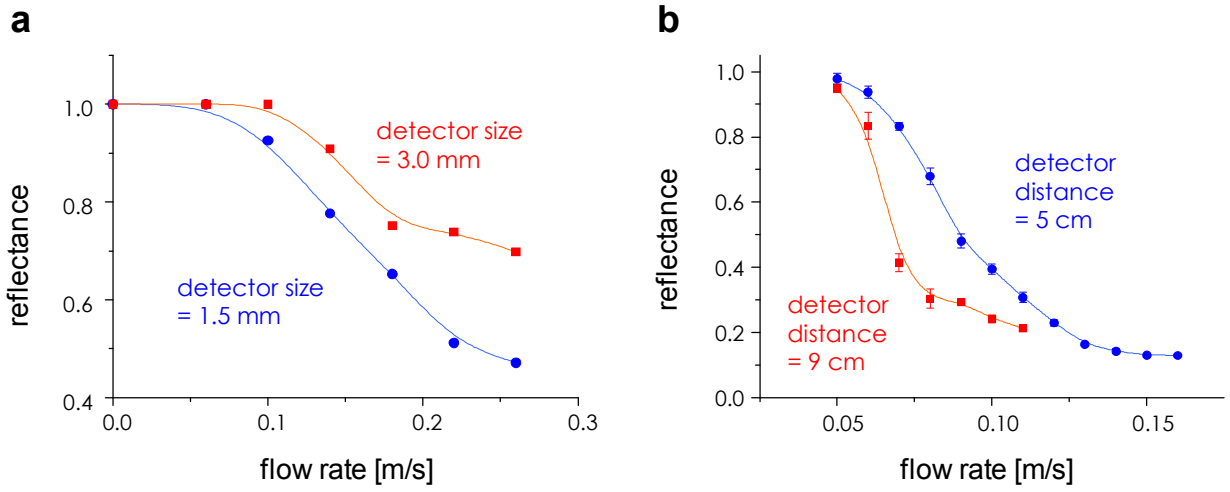

Fig. 14 The impact of detector size: (a) The simulated decrease in the MSMP's reflectance due to flow-induced bending and (b) The change in the reflectance due to the decrease in the detector area observed in MSMP-A. The error bars represent standard deviations obtained from 10 measurements.

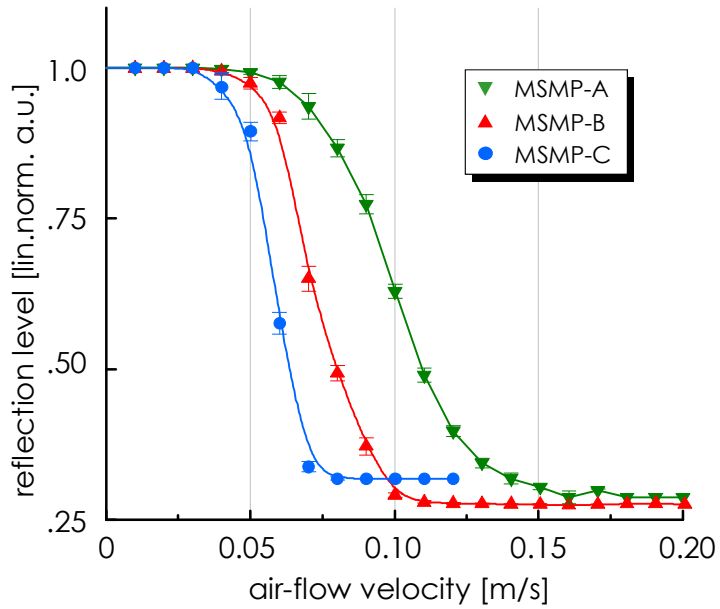

Fig. 15 The change in the micropillar's reflection level as a function of the air-flow velocity. The error bars represent the corresponding standard deviations.

Sensing of time-varying air-flows

We also investigated the utility of the MSMP for sensing air-flows with time-varying flow-rates and directions, *i.e.*, sound waves. The output of a speaker, driven by 60~200 Hz sinusoidal voltage waves, functioned as the excitation for the three MSMPs of Table 2. Figures 16a and b show the optical reflection levels from MSMP-C responding to sound waves at 60 and 90 Hz, respectively. The shades in the plots represent one temporal period. Given the sound wave driving the MSMP symmetrically, two identical dips per one temporal period were initially expected. The experimental results, however, exhibited severe asymmetry and, in the case of 60 Hz response, an extra dip. We attribute the asymmetry and the extra dip to the competition between the gradually increasing driving force and the restoration force of the PDMS micropillar. In the case of 60 Hz driving frequency, as shown in the inset of Fig. 16a, the MSMP had enough time to restore its original shape before the

driving force finally reached its maximum, pushing it back into the maximal bending. As the driving frequency increases, the extra dip diminished and disappeared eventually (Fig. 16b). The resulting generation of higher harmonics is evident in the Fourier transform of the 90 Hz response (Fig. 16c). It indicates that the reflection waveform can provide accurate information on the frequency of the acoustic excitation although it does not follow the exact excitation pattern. MSMPs A and B generated similar reflection patterns.

Figure 16d shows how the modulation-depth of the reflection output changes as a function of the excitation frequency over 60~200 Hz range. We tried our best to equalize the sound pressure at each frequency using a sound meter so that we can attribute the difference to the frequency dependence in the MSMP's level of bending. The peak frequency f_o could be easily identified for MSMP B and C as 102 and 93 Hz, respectively. The response from MSMP-A, however, did not exhibit a definite peak within the test frequency range. Since the distance between our sound source and the MSMP was much shorter than the wavelength of the sound wave, the actual patterns of air-flow around the MSMP could be much more complex than those of simple, sinusoidal waves. The analysis above may hold only at qualitative levels.

Theoretical model for the PDMS MSMP based acoustic sensors

Reports of theoretical framework for analyzing flexible micropillars with very high aspect-ratios, exceeding 40 as in the present work, are scarce. Here, we explore the effectiveness of the extended Euler-Bernoulli cantilever model for the analysis of our MSMPs. Its governing equation models the motion of a uniform, homogeneous, single-clamped cantilever beam due to a mass-flow by taking the impacts of inertia, bending, drag, and viscous damping into consideration. It has been adopted by a number of researchers for

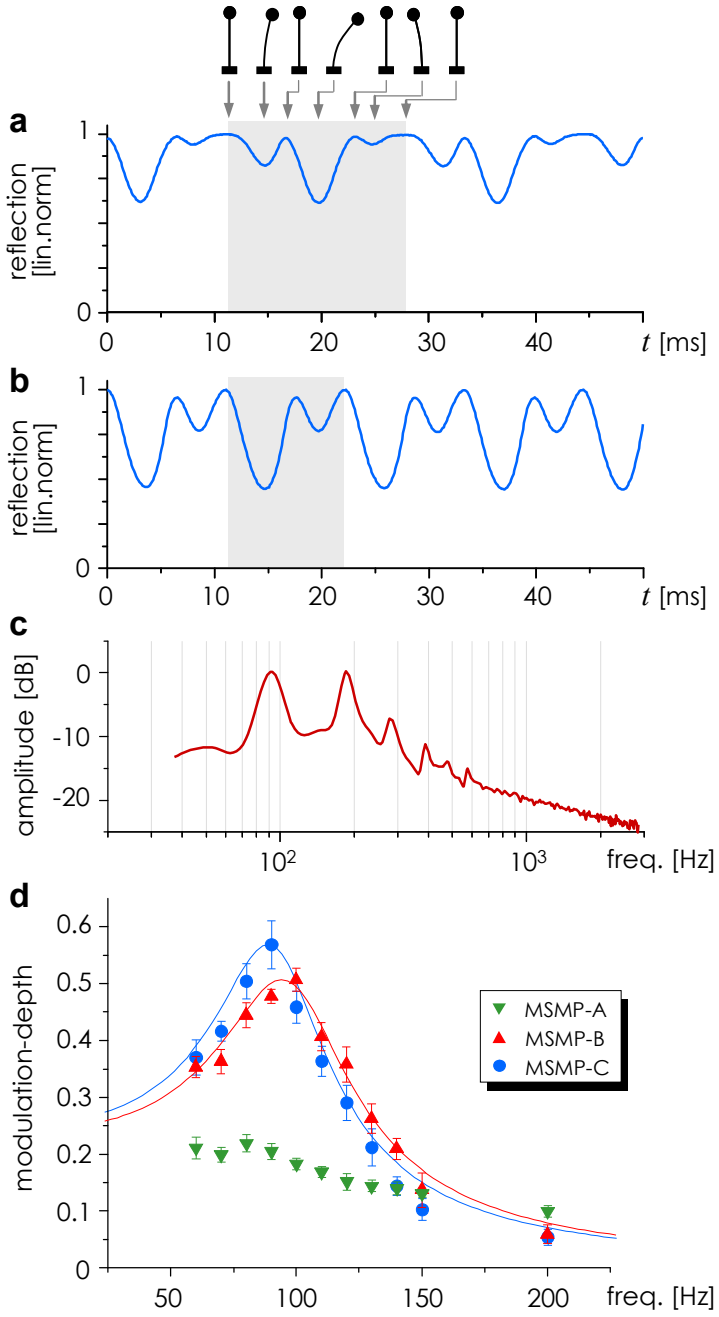

Fig. 16 Sound sensing with microsphere-tipped, high aspect-ratio PDMS micropillars: (a)-(b) Temporally changing reflections from MSMP-C in response to sound waves at (a) 60 Hz and (b) 90 Hz. The shade indicates one temporal period. The inset in (a) is to explain the origin of the appearance of extra dips in the output. (c) The amplitude portion of the Fourier transform of the 90 Hz output. (d) The modulation-depth of the temporal responses from the three MSMPs of Table 1 as a function of the excitation frequency. The solid curves represent the results of fitting the data into the frequency response of the cantilever model described in the section 3.3.3. Error bars represent the standard deviations obtained from 5 measurements.

flexible micropillars [98, 99]. Traditionally, it has been used for absolutely linear bending for which the cantilever's tip displacement is below 5% of the cantilever length. The large deflection beam theory which takes the bending into consideration as well, however, showed that the linear regime can be extended for the tip displacement up to 25% of the cantilever height [94, 95]. Since the maximum tip displacement was less than 20% of the height in our experiments, we decided to try the model. The original equation depends on both the temporal and axial variations of the cantilever. We can assume a specific axial mass-flow pattern and integrate out the axial terms, resulting in an externally driven harmonic oscillator equation,

$$m\,\partial_{tt}\,d_{tip} + c\,\partial_{t}\,d_{tip} + k\,d_{tip} = F_o\,u(t) \qquad (1)$$

,where m, c, k, F_o, and $u(t)$ are to be determined from the structural and material characteristics of the cantilever, the magnitude and waveform of the driving force, and the axial profile of the mass-flow [57]. Under the assumption of linearly varying axial loading, they are [98]:

$$m_{lin} = 60 \cdot E_Y \cdot I \,/\, (11 \cdot h^3)$$

$$c_{lin} = 52 \cdot \pi \cdot \eta \cdot h / (33 \cdot Ln(h/2/d))$$

$$k_{lin} = 13 \cdot h \cdot (A \cdot \rho_P + \chi)/33$$

,where $I = \pi/4 \cdot (d/2)^4$ is the geometrical moment of inertia, η the dynamic viscosity of air (1.81×10^{-5} Pa-s), A the cross-sectional area of the micropillar, and ρ_P the density of the micropillar material (1.05×10^{3} kg m^{-3}). The χ term represents the force due to the acceleration of the flow in the vicinity of the cantilever. Based on Ref. [100], we set χ =

$C_m \cdot A \cdot \rho_f$ where ρ_f is the density of the medium which, in our case, is air (1.2 kg m^{-3}) and C_m is the hydrodynamic mass coefficient which, in the case of a cylinder, is 1.

We also considered a constant axial mass-flow profile. Under an air-flow which maintains a constant profile along the length of the cantilever, the definitions given above become different:

$$m_{const} = 8 \cdot E_Y \cdot I \,/\, h^3$$

$$c_{const} = 8 \cdot \pi \cdot \eta \cdot h / (5 \cdot Ln(h/2/d))$$

$$k_{const} = 2 \cdot h \cdot (A \cdot \rho_P + \chi)/5.$$

Then the corresponding resonance frequency f_o and the amplitude response Y are given as:

$$f_o = (k/m)^{1/2}$$

$$Y \propto (m \cdot \omega_o^2)^{-1} \cdot [\, (1-(\omega/\omega_o)^2)^2 + (c \cdot \omega/m/\omega_o)^2 \,]^{-1/2}$$

,where $\omega_o = 2\pi \cdot f_o$.

The modeling results can be summarized as follows. First, with the structural, material, and experimental parameters given above, the harmonic oscillator model of Eq. (1) could produce resonance frequency values that are in order-of-magnitude agreements with the experimental results. For example, the computed resonance frequencies for MSMP-B and C are in the range of 40~60 Hz which is close to the measured values of 102 and 93 Hz. Second, by adjusting two material parameters, E_Y and the density of PDMS ρ_P, we could approximately reproduce the frequency responses of the two MSMPs. The results are superimposed in Fig. 16d. For MSMP-B, the best match was obtained with E_Y = 3.3 MPa and ρ_P = 525 kg m^{-3}, *i.e.*, half of the catalogue value. For MSMP-C, the best match required E_Y = 6.4 MPa and ρ_P = 525 kg m^{-3}. For MSMP-A, the shortest one, the predicted resonance frequency was 300~500 Hz. Since it was well beyond our experiment range, we did not try

curve-fitting. Third, for both MSMP-B and C, better agreements were obtained when the mass-flow rate was assumed to be increasing linearly along the MSMP's axis. Switching to the constant mass-flow profile lowered the resonance frequencies by a factor of 2 in both cases. The better match enabled by the adoption of the linearly varying flow-profile may indicate the persistent influence of the boundary layer even for cantilevers outstanding it by several hundred microns. These results indicate that application of the externally driven harmonic oscillator model to the highly flexible, high aspect-ratio PDMS micropillars could produce order-of-magnitude agreements in some output parameters. In general, however, the success was limited, necessitating more accurate numerical modeling.

Performance evaluation for the MSMP based acoustic sensors

At this point, the MSMP-based air-flow sensor's performance should be assessed and compared with those of existing PDMS-based systems. There are two aspects: First, the MSMP's effectiveness as an object interacting with an air-flow. Second, the transduction mechanism which converts the changes in the MSMP into measurable signals.

Regarding the first, the resonance frequency f_o and the bandwidth constitute the main figures of merit. In this point of view, the significance of the MSMP comes from its height and the consequential red-shift in the f_o. Replica-molded PDMS micropillars have been demonstrated by multiple researchers but their height has been limited below 700 μm with the corresponding f_o higher than 300 Hz, often in kHz range. For more versatile air-flow sensing, lower frequencies need to be covered. The present MSMP, with the longest MSMP exhibiting f_o near 100 Hz, has the potential to fill the gap. The microsphere-tipped nature of the MSMP may also enable further decrease in f_o since the extra tip-mass can slow down the cantilever dynamics [101]. Currently, as shown in Fig. 16d, the overshoot near f_o is less than

3 dB, which is reasonable for supporting wideband operation. In future designs, this flat, low-pass frequency response can be ensured through the control over the MSMP's damping mechanisms.

When it comes to the transduction performance, the sensitivity would be the main figure of merit. Those for the MSMP-based sensors have already been evaluated in the previous section. Fair comparison with other cantilever beam-based air-flow sensors [102], however, is difficult since all of them utilized piezoelectric or capacitive read-out schemes. The only systems utilizing optical read-out were the PDMS micropillar wall shear-stress sensors relying on camera-based image capture and processing [56, 99]. There, the sensitivity was defined as the ratio between the tip deflection amplitude and the wall shear stress and estimated to be ~150 μm Pa^{-1} for a 200 μm-high micropillar (20 in aspect-ratio) near 100 Hz. It was also predicted that the sensitivity would increase with the aspect-ratio in proportion to $(h/d)^{4.5} \sim (h/d)^5$. For example, the 1600 μm-high MSMP-B (72.7 in aspect-ratio) exhibited deflection amplitude close to ~20% of its height under 0.1 m s^{-1} air-flow. Under the assumption of linearly increasing air-flow velocity from the surface, the corresponding sensitivity is 0.25 m Pa^{-1}, which is in order-of-magnitude agreement with the sensitivity of the existing PDMS micropillar multiplied by $(72.7/20)^5$. To summarize, the present MSMPs exhibit sensitivity comparable to existing PDMS micropillars while bringing in additional advantages of higher aspect-ratios and lower resonance frequencies.

These sensitivity levels may be lower than those attainable with piezoelectric or capacitive read-out. Here, we emphasize the optical read-out scheme's unique advantages such as the structural simplicity, spark-free operation, and immunity to electromagnetic interference. The present scheme also exhibits advantages over existing optical read-out

schemes which rely on camera-based image capture and processing [56, 99], on the basis of its integration potential. For practical use, the reflection power measurement setup in Fig. 12a can be miniaturized and wafer-level integrated with CCD or CMOS detector arrays in an alignment-free fashion [103] using beam redirection technologies developed for board-level optical interconnect. Integrating MSMPs with diverse characteristics will also allow simultaneous sensing of multiple frequency excitations. Currently, the biggest concern is the rather high measurement threshold, evident in Fig. 15. Further modifications in the read-out configuration are required to address the issue.

Conclusion

In conclusion, I report the development of a new soft-lithography technique which allows drawing of ultra-high aspect-ratio PDMS micropillars. Despite the material's inherent softness, the technique enables routine production of upright PDMS micropillars that are 800~2400 μm in height, while suppressing their average diameters below 25 μm. The resulting aspect-ratios, ranging from 40 to 112, are unprecedented for PDMS structures standing upright on their own. A more significant feature of our new direct drawing technique is its ability to integrate microspheres at the tips of the micropillars in a self-aligned fashion. To validate the utility of the microsphere-tipped PDMS micropillar, we implement a new air-flow sensor with all-optical read-out based on it. The ultra-high aspect-ratio and the excellent flexibility of PDMS enhance the micropillars' deformation under air-flows, permitting them to exhibit mm/s-scale detection resolution in air-flow velocity. The increase in the micropillar height also lowers their resonance frequencies from the kHz range down to ~100 Hz, filling the gap in the operation bandwidth of microscale air-flow sensing.

For all those applications, the microsphere-capping capability plays an essential role by providing self-aligned reflectors to the micropillars which function as flexible waveguides, enabling the optical read-out of the micropillars' deformation. The scope of application for the self-aligned microspheres can be further expanded with judicious choices on the microspheres' size and composition. Overall, our new technique to realize microsphere-tipped high aspect-ratio micropillars will constitute a useful addition to the arsenal of soft-MEMS technology.

Acknowledgements

This work was supported by National Science Foundation through its grants ECCS1147413 and ECCS-0954845. We thank Professor L. P. Lee for valuable suggestions.

For this work, J.K. conceived the idea and supervised the research. J.P. carried out the experiments and data analyses. J.K. and J.P. co-wrote the manuscript.

.

CHAPTER 5

MICROROBOTIC TENTACLES WITH SPIRAL BENDING CAPABILITY BASED ON SHAPE-ENGINEERED ELASTIC MICROTUBE

Modified from a paper published in *Scientific Reports*

Jungwook Paek[1], Inho Cho[2], and Jaeyoun Kim[1],*

Abstract

Microscale soft-robots hold great promise as safe handlers of delicate micro-objects but their wider adoption requires micro actuators with greater efficiency and ease-of-fabrication. Here I present an elastomeric microtube-based pneumatic actuator that can be extended into a microrobotic tentacle. I establish a new, direct peeling-based technique for building long and thin, highly deformable microtubes and a semi-analytical model for their shape-engineering. Using them in combination, I amplify the microtube's pneumatically-driven bending into multi-turn inward spiraling. The resulting micro-tentacle exhibit spiraling with the final radius as small as ~185 μ m and grabbing force of ~0.78 mN, rendering itself ideal for non-damaging manipulation of soft, fragile micro-objects. This spiraling tentacle-based grabbing modality, the direct peeling-enabled elastomeric microtube fabrication technique, and the concept of microtube shape-engineering are all unprecedented and will enrich the field of soft-robotics.

[1]Department of Electrical and Computer Engineering Iowa State University, Ames, Iowa, USA. [2]Department of Civil, Construction and Environmental Engineering Iowa State University, Ames, Iowa, USA.

Introduction

Spiraling tentacles are widely utilized in nature for grabbing and squeezing objects. There have been continuous soft-robotic efforts to mimic them with pneumatic tube actuators [104, 105] but the life-like, multi-turn spiraling motion has been reproduced only by centimeter-scale tentacles so far [32, 106]. At millimeter- and sub-millimeter scales which are required for applications like *in vivo* biomedical manipulation [36-39], they could bend only up to a single-turn [41, 43, 64, 107]. Since the bending arises from the mismatch in the elongation levels of the tube's top and bottom sides, it can be amplified into spiraling through mismatch enhancement. At macroscale, it is typically done with bi-elastomeric composite structures [32] or highly modulated surface corrugations [106]. Neither is, however, easy to implement at microscale.

Here, our approach is two-stepped. In the first, I fabricate easily deformable elastomeric microtubes as the platform structure. High deformability is ensured by the thinness of the microtube itself (100− 125 μm in inner diameter) and its tube-wall (8− 32 μm). Making such a subtle structure at a length exceeding several millimeters has been deemed unfeasible. I accomplish it with a new, direct peeling-based soft-lithographic technique. It also allows significant asymmetrization of the microtube's cross-sectional shape which leads to bending up to a single-turn. In the second step, I apply shape-engineering to the microtube to amplify the bending into multi-turn spiraling. Using a semi-analytical model, I establish a design rule which enables such a spiraling with a simple hump (Fig. 17a). The outcome is a soft-robotic micro-tentacle that can wind around and hold fragile micro-objects with ~200 μm final spiral radius. This spiraling micro-tentacle manipulator,

along with the shape-engineering concept and microtube fabrication technique, are all unprecedented and poised to enrich the field of soft-robotics.

Fabrication of PDMS Microtube based Soft-Robotic Tentacles

Past reports testify that the biggest issue in using liquid-phase poly(dimethylsiloxane) (PDMS) for building long and thin structures, such as pillars or wires, is its tendency to bead [108]. In my previous work, I fabricated ultra-high aspect-ratio PDMS micropillars by suppressing the beading with pre-curing and in situ thermal solidification [109]. Here, I extend the technique to liquid-phase PDMS dip-coated around cylindrical templates to realize PDMS microtubes with very thin walls without bonding (Fig. 17b, c).

As depicted in Fig. 17b, I started out with the preparation of the cylindrical template. Sodium dodecyl sulfate (SDS, Fisher Scientific), a surfactant, was mixed with water at 1:10 weight ratio. Then I treated a cylindrical template with the surfactant solution by dipping it into the mixture for 10 minutes. I used short sections of ~100 μm-diameter polyamide wire (Stroft ABR, Stroft) and 125 μm-diameter fused silica optical fiber (SMF-28, Corning) as the cylindrical template. The former turned out to be better in realizing multi-turn spiraling micro-tentacles with smaller final RoCs when compared with the latter. In parallel, I prepared a thin layer of PDMS by dispensing a drop of liquid-phase PDMS into a rectangular, 167 μm-deep recess on a glass substrate and removing the excess PDMS with a miniature squeegee. Then, I pre-baked the PDMS thin film with a hot plate set at 70 °C for 8 minutes and left it at room temperature for 30 minutes. Upon the completion of pre-baking, I immersed the surfactant-treated template into the PDMS thin film and dip-coated it with PDMS. The PDMS-coated template was then post-baked at 130 °C for 10 minutes. During

the post-bake, gravity induced the PDMS under baking to flow downward, giving eccentricity to the cross-sectional shape of the PDMS coating. After the post-bake, I peeled the PDMS layer off the template using a standard optical fiber jacket remover (F-STR-103D, Newport). The completed PDMS microtube is robust enough to be peeled directly from the template with a polymer jacket remover, a standard tool in fiber-optics (Figs. 17d).

The process is simpler, cleaner, and faster than those requiring dissolvable templates [18, 80]. Using polyamide wires (~100 μm diameter) and glass optical fibers (125 μm diameter) as the template, we fabricated microtubes with their length L reaching 5− 8 mm. The main factor limiting L was the inevitable increase in the friction and wrinkling during the peeling process. Despite their high aspect-ratios (typically > 50) and thin walls, the microtubes did not sag or collapse, even when no air pressure was applied. The solidification process can also be controlled for additional tailoring of the microtube's cross-sectional shape. Slowing it down prolongs gravitational impact on the coating, resulting in an increase in the tube's cross-sectional asymmetry, as shown in Fig. 17e. The 10 samples we fabricated with the 100 μm-diameter template exhibited t_1 and t_2 of 31.8 ± 4.9 (s.d.) and 7.9 ± 1 (s.d.) μm, respectively. The coating thickness can also be made uniform by rotating the template during curing.

As shown in Fig. 17f, I then placed the completed eccentric PDMS microtube on a pre-made PDMS block, poured liquid-phase PDMS, and then cured the whole assembly on a hot plate set at 130 °C for 10 minutes. I also closed the open-end of the microtube by dispensing a PDMS droplet for hermetic sealing. Finally, I dispensed a 35 nL PDMS droplet on the exterior of the microtube to realize a monolithically integrated hump structure. I exploited this capability extensively to shape-engineer the microtube.

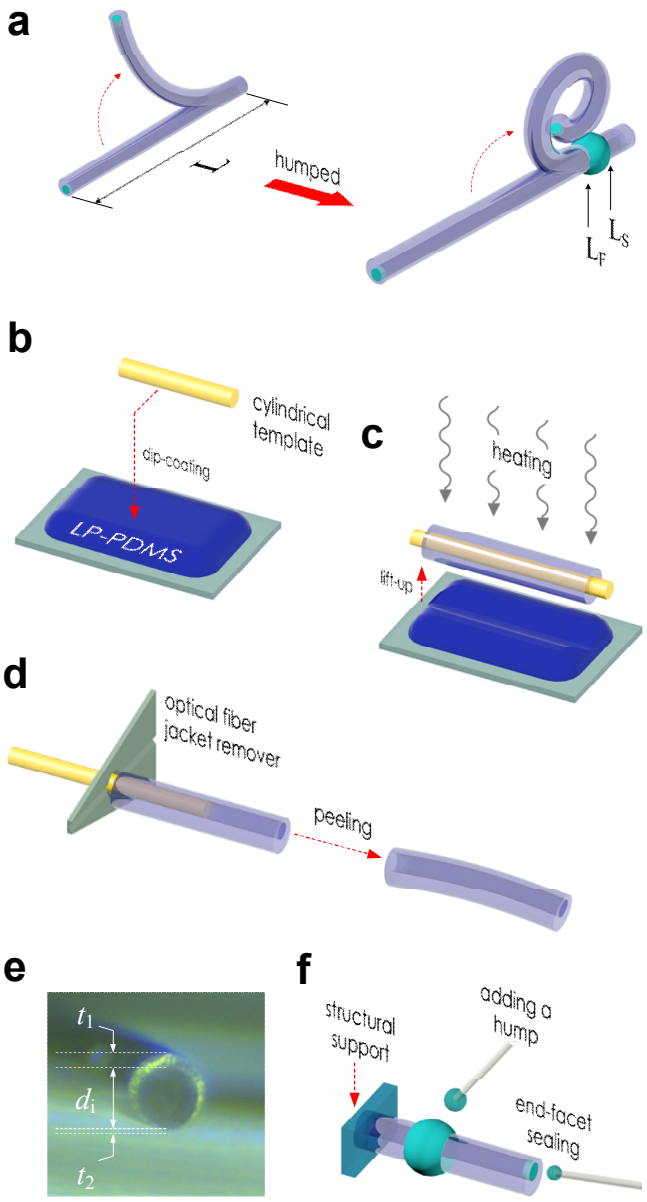

Fig. 17 PDMS microtube tentacle actuator and its fabrication: (a) A schematic diagram of PDMS microtube tentacle actuator. Unlike the plain microtube (left), the one shape-engineered with a hump (right) can produce a tentacle-like spiraling motion. Fabrication steps: (b) Dip-coating of a cylindrical template with liquid-phase (LP) PDMS, (c) Lifting up of the PDMS-coated template with *in situ* heating, (d) Peeling of the cured PDMS microtube with a fiber-optic jacket remover, (e) The cross-sectional optical micrograph of a microtube shows the gravity-induced asymmetry ($t_1 \neq t_2$). (f) Additional structures, such as the mount, end-facet sealing, and hump, can be installed to the already completed and tested microtube.

Pneumatic Actuation of PDMS Microtubes

We connected the microtubes directly to blunt syringe needles for pneumatic actuation. Owing to their high aspect-ratio, thin tube-wall, and inherent softness of PDMS, the microtubes bent significantly upon applying air pressure, as shown in Fig. 18a, b. As the characterization sample, we used the one in Fig. 18a (MT1) with L, d_i, t_1, and t_2 at 5600, 104, 35.6, and 7.7 μm, respectively. Figure 18c shows the levels of its axial elongation and radial expansion at different pressure levels. Clearly, the two morphological changes occurred with a common threshold in the applied pressure (~4.7 psi) below which they became negligible. Beyond the threshold, both the length and radius changed rapidly, eventually getting increased by 5% and 18%, respectively. Such large deformations caused the cross-sectionally asymmetric microtube to bend. Figure 18d and its inset show the decrease in MT1's radius of curvature (RoC) which also changed abruptly as the pressure surpassed the threshold value. The RoC of MT1 saturated at 1.3 mm at 8.3 psi, forming a ring as shown in Fig. 18a. Other microtubes exhibited similar responses.

Regardless of the pressure or cross-sectional asymmetry, plain microtubes with no cross-sectional change along in the axial direction failed to achieve spiraling. Conventionally, such an insufficient bending has been amplified into spiraling through the use of bi-material composite structures [32] or bellows-like surface corrugations [106, 110] which promote the mismatch in the elongation capabilities. They are, however, very complex to implement at microscale.

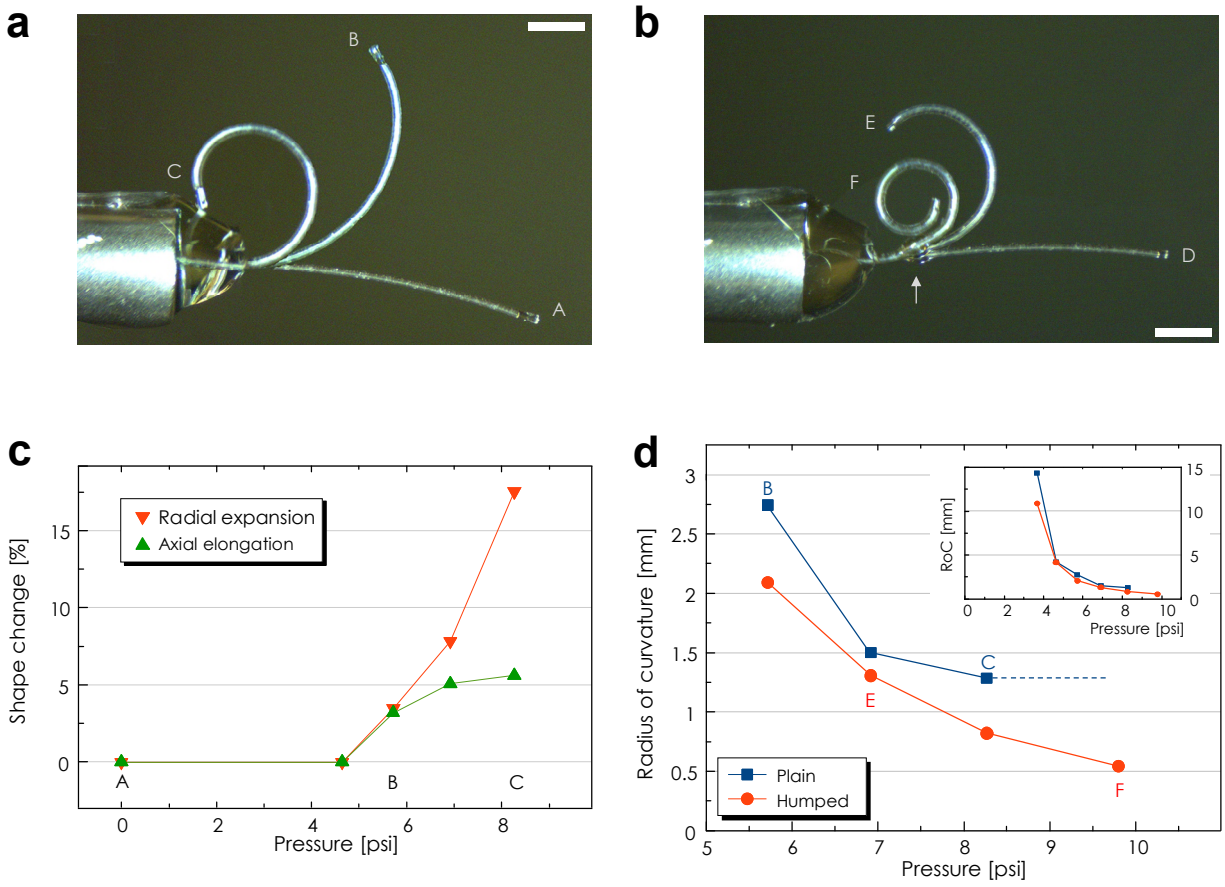

Fig. 18 Pneumatic actuation of PDMS microtubes: Superimposed images of pneumatically actuated PDMS microtube MT1. Labels A-F indicate pressure levels marked in Figs. 18c and d. The cylinder on the left-hand side is a blunt syringe needle with 2.108 mm outer diameter. (a) Before adding a hump, its bending did not develop into spiraling. (b) Adding a hump at the arrow point amplified MT1's bending into spiraling. (Scale bars: 1 mm) (c) Axial and radial shape changes observed in MT1 (before adding the hump) as a function of pressure. (d) Changes in MT1's RoC. Without the hump, it saturated at ~1.3 mm. The hump reduced it to ~500 μm. The inset shows that the RoC decreased rapidly once the pressure surpassed the threshold value at ~4.7 psi.

Shape-Engineering for Tentacle Motion

Here, we enabled the spiraling motion in the PDMS microtube actuator by adding a simple hump to it as shown in Figs. 17f and 18b. In terms of fabrication, this approach is highly advantageous since it requires access only to the microtube's exterior and, hence, can be executed after the microtube is completely fabricated and tested. Figure 18b shows the change in MT1's pneumatic actuation after a 610 μm-long, 96 μm-high hump was added. It clearly exhibited spiraling with the minimum RoC reduced to 500 μm.

We investigated the hump's role in promoting the spiraling motion using the Euler-Bernoulli beam theory [64, 111, 112]. At the instant when the microtube nearly forms a ring shape, the coordinates (x, y) of the deformed base curve can be described by an integration:

$$u(s) = \int_0^s f\left(\int_0^{s'} \frac{M_o}{E \cdot I(\eta)} d\eta\right) ds' \tag{2}$$

where s ∈ [0, L] is the natural coordinate of the beam of length L, and f is a cosine (sine) function for u = x (u = y). E is the material's Young's modulus, and I is the second moment of area. At this specific instant, it is plausible to assume that a plain microtube has a constant I along its length, and that a humped microtube has a step-wise distribution of I, as shown in Fig. 19a. Herein, we restrict our qualitative investigation to elastic regime at an instant with a fixed pressure. The full evolution of I with increasing pressure would call for analyses of hyperelastic deformations and plasticity at extreme cases, which is beyond our scope. The bending moment $M_o \equiv \pi \cdot r^2 \cdot p \cdot d_e$ where r is the radius, p the current pressure, and d_e the distance between the microtube's neutral axis and void hole's center. Figure 19b shows that the plain microtube will bend gradually to form a ring but will not achieve spiraling. It is clear from the plot that an inward spiraling requires re-entry of the end-point into the first

quadrant with its y > 0. In light of the simple harmonic functions in equation (2), the integration over a full cycle will reset both x and y to 0, thereby impeding the desired spiraling.

With the hump, we can modulate the microtube's geometry and, hence, the values of I as shown in Fig. 19a. Considering the step-wise distribution of I, the integration in equation (2) will be split into three, each covering the pre-hump, hump, and post-hump sections as:

$$u(s < L_S) = \int_0^s f\left(\frac{M_o \cdot s'}{E \cdot I_o}\right) ds' \tag{3}$$

$$u(L_S \le s < L_F) = \int_0^s f\left(\frac{M_o \cdot s'}{E \cdot I_1} + \frac{M_o \alpha L}{E} \cdot \left(\frac{1}{I_o} - \frac{1}{I_1}\right)\right) ds' \tag{4}$$

$$u(L_F \le s < L) = \int_0^s f\left(\frac{M_o \cdot s'}{E \cdot I_o} - \frac{M_o \beta L}{E} \cdot \left(\frac{1}{I_o} - \frac{1}{I_1}\right)\right) ds' \tag{5}$$

Where I_1 and I_0 are the values of I in the hump and non-hump sections, respectively, as shown in Fig. 19a. The position and length of the hump are also specified through α and β in Fig. 19a. Equations (2)-(4) and Fig. 20 show that the sinusoidal functions in the integrands will obtain abrupt phase shifts when $I_0 < I_1$. By adjusting the levels of the phase-shifts in *x* and *y*, we can control re-entry point to the first quadrant. A simple criterion can be derived by assuming $L \cdot \beta\,(I_1 - I_o)/I_1 \ll L\,/\,4$. In that case, spiraling can be ensured with $\beta \cdot (I_1 - I_o)/(2 \cdot I_1) < \alpha < 0.5 + \beta \cdot (I_1 - I_o)/(2 \cdot I_1)$.

Figures 19b and c show how a hump (length = 0.05·L) affects the level of bending as a function of its position. We used a microtube model with its characteristics approximately matching those of MT1. With I_0 and I_1 at 5.1 × 10−16 and 8.6 × 10−15 m^4 , respectively, the inward spiraling can be obtained when 0.024 < α < 0.524. We set the α value of Hump B at

an improper value of 0.55 while setting that of Hump A to the proper value of 0.21, as indicated by arrows in Fig. 19c. Despite their identical size and shape, the two humps impacted the microtube's bending very differently. As predicted, Hump A did achieve inward spiraling with the final $y > 0$. Hump B, on the other hand, performed even worse than the plain, un-humped microtube, resulting in $y < 0$.

To experimentally confirm the prediction above, we fabricated another PDMS microtube with structural characteristics very similar to those of MT1 with L, d_i, t_1, and t_2 at 5800, 104, 33, and 7.4 μ m, respectively, and compared its bending behaviors before and after adding a hump at an obviously improper position of 0.78·L. Figure 3d shows the results. In good agreement with the theoretical prediction, the improperly positioned hump resulted in bending radius even greater than that of its non-humped prototype.

Figure 19e, on the other hand, shows one of the best spiraling results observed so far. As shown in the optical micrograph, the optimized microtube actuator, with L, d_i, t_1, and t_2 at 5470, 105, 34.6, and 8.2 μm, respectively, and its hump installed at 0.17·L point exhibited spiraling with two full turns, achieving the final RoC of 210 μm. RoC as low as 185 μm has been obtained.

Characterization of Micro-Tentacle Actuation and Discussion

Characterization of micro-tentacle actuation

The spiral formed by the PDMS micro-tentacle is ideal for grabbing and holding microscale objects. To estimate its grabbing force, we configured it to deflect a cantilever as shown in the inset of Fig. 21a. As the cantilever, we used a 15 mm-long section of 125 μm-diameter fused silica optical fiber. We also installed a rigid, 155 μm-diameter metal wire in

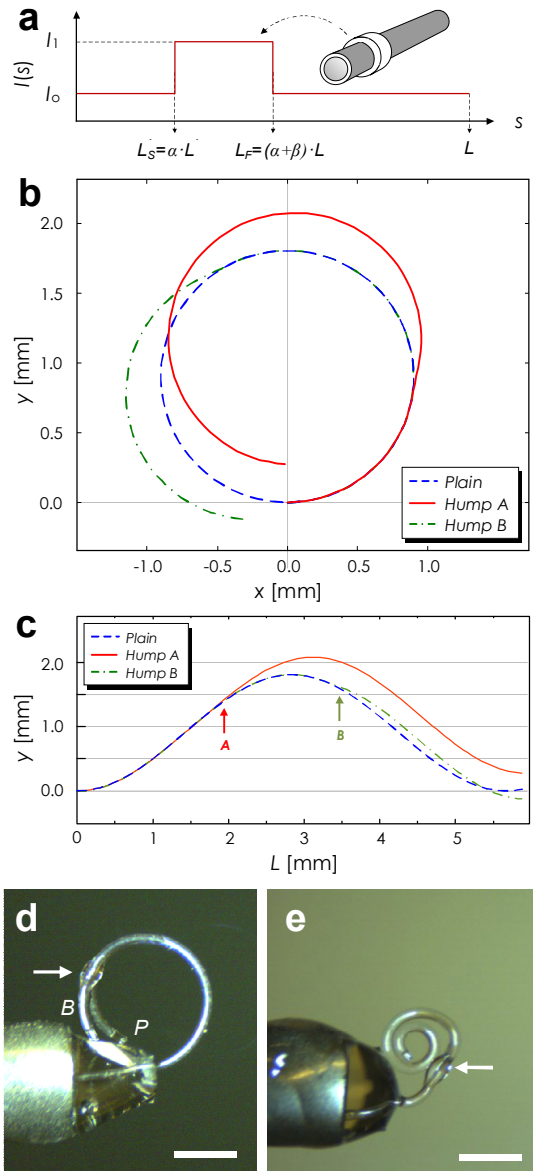

Fig. 19 Shape-engineering of PDMS micro-tentacles: (a) A schematic diagram of a humped PDMS micro-tentacle and the change inits *I* due to the hump. Calculated loci (b) and *y*-values (c) of three microtubes with different hump configurations. *Plain*: no axial change in cross-sectional shape, *Hump A*: with a properly positioned hump ($L_s = 0.21 \cdot L$), and *Hump B*: with an improperly positioned hump ($L_s = 0.55 \cdot L$). *Hump A* re-entered the first quadrant with$y > 0$, achieving an inward spiraling. *Hump B*, on the other hand, actually renderedthe bending worse than that of the non-humped *Plain*. (d) Overlapped images of microtube actuations before (*P*) and after (*B*) installing an improperly positioned hump (arrow-marked). The RoC got bigger even with the hump. (e) Micrograph of a micro-tentacle with a hump (arrow-marked) capable of achieving a 2-turn spiraling with the final RoC of 210μm. (Scale bars: 1mm)

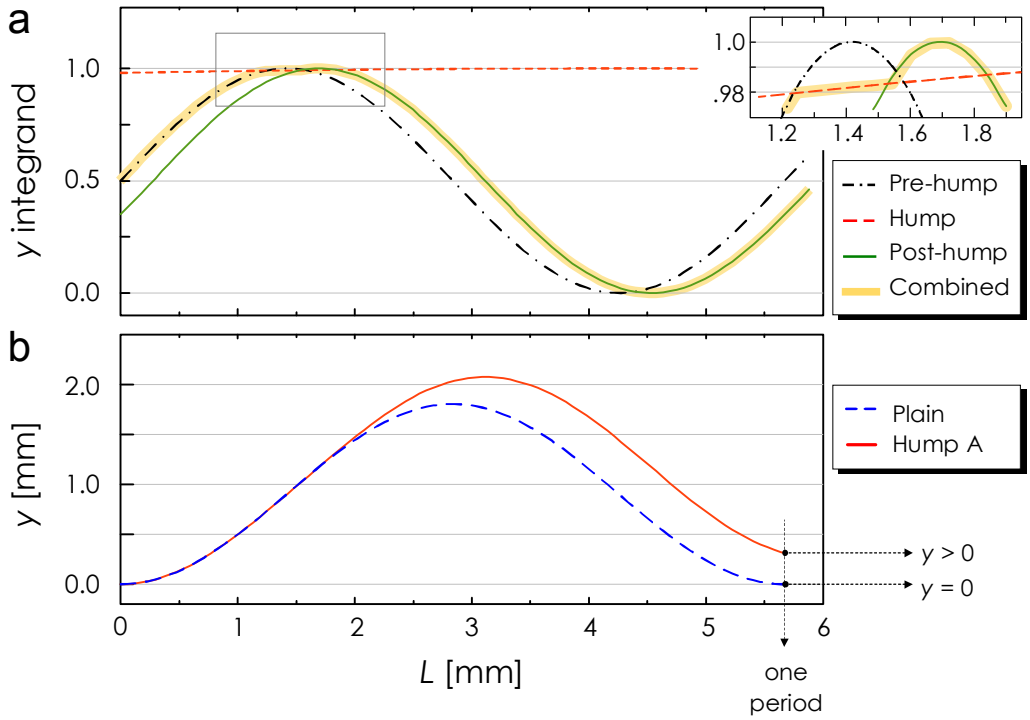

Fig. 20 Changes in the integrands due to the hump: (a) The changes in the y-integrands for the pre-hump, hump, and post-hump sections specified in Eqs. (2)-(4), respectively. For the humped microtube, the integration must be performed along the highlighted "combined" route, *i.e.*, first along the pre-hump curve (black, dash-dot), then the hump curve (red, dashed), and then the post-hump curve (green, solid). For the un-humped one, it suffices to integrate along the pre-hump curve. (b) The integration results for the plain, un-humped microtube (blue, dashed) and the humped one (red, solid). For the integration over a full cycle, the purely sinusoidal integrand of the former ended up $y = 0$. In contrast, with $I_1 >> I_o$, the hump section curve changes much more slowly than those in other sections and can function as a phase-shift between them (as shown in the inset in detail), eventually altering the integration result to a non-zero, positive value. This enables the inward spiraling of the micro-tentacle.

parallel with the fiber. Their surface-to-surface separation was 290 μm. Then, we wound the micro-tentacle around both the metal wire and optical fiber so that its grabbing force can function as a point load at h_g to the optical fiber cantilever. The standard beam deflection theory relates the force F and the deflection δ_c at h_g as:

$$\delta_c = \frac{F \cdot h_g^3}{3 \cdot E \cdot I} \tag{6}$$

,where $I = \pi r^4/4$, r the radius of the optical fiber cantilever, and E the Young's modulus of fused silica.

For this measurement, we used a micro-tentacle with L, d_i, t_1, and t_2 at 5000, 107, 39.1, and 7.2 μm, respectively. Its minimum spiraling diameter was 370 μm and the corresponding maximum achievable deflection $\delta_{c,max}$ was 200 μm. Figure 21a shows the measured values of δ_c as a function of h_g at the pressure level of 9.8 psi. Each represents the average of five measurements. We omitted the error bar since the standard deviations were < 1% of the average values. The force F, estimated through curve-fitting, was approximately 0.78 mN. We considered only the first four points in the curve-fitting since δ_t approached its maximum possible value and began to saturate beyond $h_g \sim 7.5$ mm.

Thanks to the softness of PDMS and the spiraling motion, the micro-tentacle can function as a soft-robotic grabber of micro-objects that can easily be deformed or damaged under those made of hard materials. As practical examples, we attempted to grab biological objects. We utilized a micro-tentacle with L, d_i, t_1, and t_2 at 5000, 104, 31.5, and 6.9 μm, respectively. Our first target was the egg of capelin (*Mallotusvillosus*) which deforms and bursts easily when manipulated with hard tweezers. We initially placed multiple eggs on a

glass slide and then used the micro-tentacle's bending motion to separate one egg. Then we grabbed the egg by winding the micro-tentacle around it. The optical micrographs in Figs. 21b and c were obtained while the egg was being held up by the micro-tentacle. In particular, Fig. 21b shows that the micro-tentacle conformally wound itself around the irregularly shaped egg, giving it minimal mechanical stress. We observed no sign of deformation after we released the egg. As shown in Fig. 21d, we also grabbed and held an ant (approximately 400μm across the waist) without damaging its body as well.

Discussion

The cantilever deflection measurement revealed that the spiraling micro-tentacle's grabbing force is in the vicinity of 0.78 mN at 9.8 psi pneumatic pressure. In absolute sense, this force is weaker than those of existing elastomer-based pneumatic micro-actuators. For example, the PDMS/polyimide-based pneumatic balloon actuator by Konish et al. exhibited 10 ~ 50 mN of force [113]. Smaller elastomeric micro-manipulators reported by Watanabe et al. and Wakimoto et al. also exhibited force levels of 3 mN [40] and 2.2 mN [41] , respectively. When dealing with microscale actuators, however, their size must be taken into consideration as well. The force-volume ratios for the three actuators above are 0.78, 3.3, and 0.047 mN/mm^3, respectively. The force-volume ratio of our micro-tentacle is 8.4 mN/mm^3 which is higher or comparable to those listed above. It indicates that our micro-tentacle produced force very efficiently with a simple and small structure. In fact, our micro-tentacle can be regarded as the bridge between the conventional, larger micro-actuators producing mN-level force and biological micro-organisms such as C. elegans capable of producing 62 μN of force [114]. Given that multi-cell aggregates exhibit resilience against force at least up

to 1 mN [42], the sub-mN force level of the micro-tentacle can be highly useful for biomedical cellular manipulation.

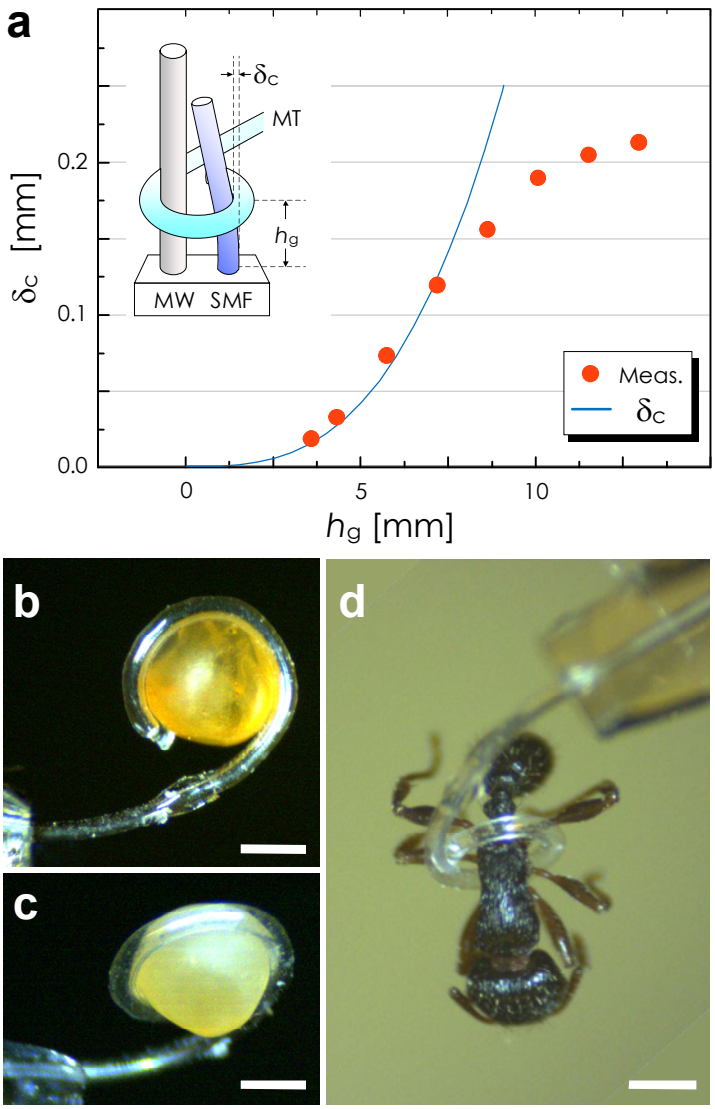

Fig. 21 Characterization of PDMS micro-tentacle actuation: (a) Measured deflection of the cantilever due to the PDMS micro-tentacle's grabbing force. The inset shows the experimental setup (MW: metal wire, SMF: glass optical fiber, MT: micro-tentacle). The solid line represents δ_c, the deflection at the grabbingpoint (h_g), calculated based on the standard beam deflection theory with the point-loaded force of 0.78mN.The measured δ_c begins to deviate from the theory after it exceeds 90 μm, the maximum stroke achievable with the current setup. (b) and (c) Optical micrographsshowing the micro-tentacle's ability to grab and hold a*Mallotusvillosus*egg by winding around it conformally. (d) Optical micrograph of another micro-tentacle grabbing and holding an ant. (Scale bar: 500 μm for all)

Conclusion

To conclude, I have demonstrated elastomer-based soft-robotic micro-tentacles capable of winding around and holding microscale objects. To realize the thin, highly deformable microtubes, I established a new fabrication technique based on in situ thermal solidification of PDMS dip-coated around a cylindrical template and direct peeling of the cured structure. Its capability to asymmetrize the microtube's cross-sectional shape enabled the microtube to bend up to a single turn. But I went further to amplify the bending into a life-like, multi-turn spiraling motion. To that end, I established a semi-analytical model to shape-engineer the microtube and turn it into a micro-tentacle. The optimized micro-tentacle exhibited a spiraling motion with two full turns and ~200 μm inner radius, which is ideal for grabbing micro-objects.

Experimental confirmation of the feasibility of such a winding motion in elastomer-based microscale pneumatic actuators is another of this study's contribution. The spiraling capability will render the micro-tentacle particularly useful for manipulating fragile or easily deformable objects since it will allow the micro-tentacle to grab and hold a delicate object either by winding around it conformally or by forming a ring that can scoop up the object without squeezing. Thanks to the use of PDMS for its construction and also to its microorganism-level force, our micro-tentacle is fully compliance-matched to biological structures [29] and will be ideal for future in vivo biomedical manipulation or surgery [36, 37] and endovascular operations [43, 115] where tissue safety holds the highest priority.

Acknowledgements

J.P. and J.K. were supported by National Science Foundation through its grants ECCS-0954845. I.C. gratefully acknowledges the research support from CCEE of ISU.

For this work, J.K. conceived the idea, supervised the research, and performed data analysis. IC established the semi-analytical model for shape-engineering. J.P. established the fabrication protocols and performed the characterization. All authors co-wrote the manuscript.

CHAPTER 6

SUMMARY AND CONCLUSIONS

In conclusion, I have successfully demonstrated new micro-fabrication schemes for unconventional, elastomer-based microsystems and their applications.

First, I established a simple and novel fabrication scheme which enables the realization of 3D networked, cylindrical MF channels by adopting sucrose as the sacrificial material. The sucrose fiber templates exhibit chemical, mechanical, and thermal characteristics suitable for their shaping, bonding, and assembly, enabling the realization of essential 3D MF channel architectures such as cylindrical tapers, internal looping, end-to-side junctions, tapered junctions, and local stenosis, which are difficult when attempted with existing schemes. The last two will especially benefit vaso-mimetic efforts, hemodynamic studies, and 3D tissue scaffolding. On top of that, the scheme is based on only low temperature, water dissolution process so that it is environment friendly and cost effective.

As potential applications of the MF channels for PoC monitoring, I have successfully demonstrated the integration of the *bokeh* microscopy with microfluidics. For this work, MF channels were realized based on our proprietary fabrication technique and then, a single microlens was installed over the microfluidic side. The microlens-generated image capturing was achieved by an ordinary, widely available camera. Analysis of the resulting magnified images of MF channel and its contents indicate that this simple microscopy scheme is capable of providing 10~40 of magnification and 67~252μm of field-of-view extent, which are adequate for monitoring 50~100 μm microchannels carrying 10~50 μm objects. Thanks to the inherent simplicity of the *bokeh* microscopy scheme and its fabrication techniques, the

implementation of the bokeh microscopy integrated with the MF channels greatly facilitates its use for PoC applications in highly resource limited environment.

On top of that, I report a new technique which enables the realization of PDMS micropillars with ultra-high aspect-ratio. The incorporation of *in situ* thermal hardening with the direct-drawing technique was the key enabler. With the technique, I routinely produced micropillars with their mm-scale height and μm-scale diameter, achieving aspect-ratios in the range between 57 and 112, which is unprecedented for elastomers such as PDMS. The scheme also differentiates itself from other direct-drawing techniques in its use of detachable microspheres as the drawing probes which allows self-aligned capping of the micropillar with microspheres possessing various functionalities. As a validation of the microsphere-tipped PDMS micropillar's utility, I turned it into an optical air-flow sensor. Its high aspect-ratio, together with the excellent flexibility of PDMS, allowed the micropillar to deform significantly even under weak air-flows, leading to mm/s-scale detection resolution. The increase in the micropillar's height also lowered their resonance frequency from the usual kHz range down to ~100 Hz, filling the gap in the operation bandwidth of microscale air-flow sensing. The microspheres, on the other hand, were utilized as compact, self-aligned mirrors which guarantee maximal reflection during optical read-out of the micropillar's deformation. Overall, both the microsphere-tipped high aspect-ratio micropillar architecture and its fabrication technique will constitute useful additions to the toolbox of soft-MEMS technology, with their utility and success hinged on the choice of the microspheres' size and composition.

Finally, I have demonstrated elastomeric microtube based soft-robotic tentacles capable of grabbing and holding microscale objects. For this work, I established a new

fabrication technique which allows the realization of high aspect-ratio elastomeric microtubes with very thin walls based on *in situ* thermal solidification of PDMS dip-coated around a cylindrical template and direct peeling of the cured structure. It also allows significant asymmetrization of the microtube's cross-sectional shape which leads to bending up to a single-turn. Then, I shape-engineered the microtube to amplify its bending into multi-turn spiraling. Using a semi-analytical model, I established a design rule which enables such a spiraling with a simple hump. The outcome exhibited a spiraling motion with a final radius of ~185 μm and 0.78 mN of squeezing force, which are ideal for grabbing micro-objects that can easily be deformed or damaged.

In summary, I have actively researched on realizations of unconventional elastomeric structures by devising novel, simple, and cost-effective fabrication schemes. And I believe that the outcomes will constitute a useful toolbox for diverse research areas. For example, the high aspect-ratio PDMS micropillar which can function as a standing-upright flexible waveguide and its fabrication scheme can benefit not only soft-MEMS research area but also optics related studies by paving a new road for freestanding elastomeric optics, escaping from the rigid, inelastic optics, which will, in turn, widen the scope of optical applications.

REFERENCES

[1] H. Wu, T. W. Odom, D. T. Chiu and G. M. Whitesides, "Fabrication of Complex Three-Dimensional Microchannel Systems in PDMS," J. Am. Chem. Soc., 2003, 125, 554–559.

[2] Y. Luo and R. N. Zare, "Perforated membrane method for fabricating three-dimensional polydimethylsiloxane microfluidic devices," Lab Chip, 2008, 8, 1688–1694.

[3] K.-S. Yun and E. Yoon, "Fabrication of complex multilevel microchannels in PDMS by using threedimensional photoresist masters," Lab Chip, 2008, 8, 245–250.

[4] M. Abdelgawad, C. Wu, W.-Y. Chien, W. R. Geddie, M. A. S. Jewett and Y. Sun, "A fast and simple method to fabricate circular microchannels in polydimethylsiloxane (PDMS)," Lab Chip, 2011, 11, 545–551.

[5] S. H. Lee, D. H. Kang, H. N. Kim and K. Y. Suh, "Use of directly molded poly(methyl methacrylate) channels for microfluidic applications," Lab Chip, 2010, 10, 3300–3306.

[6] A. Asthana, K.-O. Kim, J. Perumal, D.-M. Kim and D.-P. Kim, "Facile single step fabrication of microchannels with varying size," Lab Chip, 2009, 9, 1138–1142.

[7] J. T. Borenstein, M. M. Tupper, P. J. Mack, E. J. Weinberg, A. S. Khalil, J. Hsiao and G. Garcia Cardena, "Functional endothelialized microvascular networks with circular cross-sections in a tissue culture substrate," Biomed. Microdevices, 2010, 12, 71–79.

[8] J. T. Borenstein and G. Vunjak-Novakovic, "Engineering tissue with BioMEMS," IEEE Pulse, 2011, 2, 28–34.

[9] E. C. Novosel, C. Kleinhans and P. J. Kluger, "Vascularization is the key challenge in tissue engineering," Adv. Drug Delivery Rev., 2011, 63, 300–311.

[10] L. K. Fiddes, N. Raz, S. Srigunapalan, E. Tumarkan, C. A. Simmons, A. R. Wheeler and E. Kumacheva, "A circular cross-section PDMS microfluidics system for replication of cardiovascular flow conditions," Biomaterials, 2010, 31, 3459–3464.

[11] R. Lima, M. S. N. Oliveira, T. Ishikawa, H. Kaji, S. Tanaka, M. Nishizawa and T. Yamaguchi, "Axisymmetric polydimethysiloxane microchannels for in vitro hemodynamic studies," Biofabrication, 2009, 1, 035005.

[12] J. Hanzlik, E. Cretekos and K. A. Lamkin-Kennard, "Biomimetic Leukocyte Adhesion: A Review of Microfluidic and Computational Approaches and Applications," J. Bionic Eng., 2008, 5, 317–327.

[13] A. del Campo and E. Arzt, "Fabrication approaches for generating complex micro- and nanopatterns on polymer surfaces," Chem. Rev. 108, 911 – 945, 2008.

[14] W. Chen, R. H. W. Lam, and J. Fu, "Photolithographic surface micromachining of polydimethylsiloxane (PDMS)," Lab Chip, 12, 391 – 395, 2012.

[15] P. Ferraro, S. Coppola, S. Grilli, M. Paturzo, and V. Vespini, "Dispensing nano-pico droplets and liquid patterning by pyroelectrodynamic shooting," Nature Nanotech. 5, 429 – 435, 2010.

[16] Y. Zhao and H. Zeng, "Fabrication of non-photodefinable polymer microstructures for micro-total-analysis," Sensors and Actuators B, 139, 673 – 681, 2009.

[17] J. Lee and J. Kim, "Fabrication of strongly anchored, high aspect-ratio elastomeric microwires for mechanical and optical applications," J. Micromech. Microeng. 21, 085016, 2011.

[18] J. Lee and J. Kim, "Elastomeric microwire-based optical gas flowmeter with stretching-enabled tunability in measurement range," Opt. Lett. 36, 3789 - 3791, 2011.

[19] R. Madugani, Y. Yang, J. M. Ward, J. D. Riordan, S. Coppola, V. Vespini, S. Grilli, A. Finizio, P. Ferraro, and S. N. Chormaic, "Terahertz tuning of whispering gallery modes in a PDMS stand-alone, stretchable microsphere," Opt. Lett. 37, 4762 - 4764, 2012.

[20] S. Grilli, S. Coppola, V. Vespini, F. Merola, A. Finizio, and P. Ferraro, "3D lithography by rapid curing of the liquid instabilities at nanoscale," PNAS, 108, 15106 – 15111, 2011.

[21] K. Oh, J.-H. Chung, S. Devasia, and J. J. Riley, "Bio-mimetic silicone cilia for microfluidic manipulation," Lab Chip, 9, 1561 – 1566, 2009.

[22] D. Sameoto and C. Menon, "A low-cost, high-yield fabrication method for producing optimized biomimetic dry adhesives," J. Micromech. Microeng. 19, 115002, 2009.

[23] L. Courbin, E. Denieul, E. Dressaire, M. Roper, A. Ajdari, and H . A. Stone, "Imbibition by polygonal spreading on microdecorated surfaces," Nature Mat. 6, 661 – 664, 2007.

[24] J. L. Tan, J. Tien, D. M. Pirone, D. S. Gray, K. Bhadriraju, and C. S. Chen, "Cells lying on a bed of microneedles: An approach to isolate mechanical force," PNAS, 100, 1484 – 1489, 2003.

[25] S. P. Sane and M. J. McHenry, "The biomechanics of sensory organs," Integr. Comp. Biol. 49, i8 - i23, 2009.

[26] J. Tao and X. Yu, "Hair flow sensors: from bio-inspiration to bio-mimicking – a review," Smart Mater. Struct. 21, 113001, 2012.

[27] M. E. McConney, K. D. Anderson, L. L. Brott, R. R. Naik, and V. V. Tsukuruk, "Bioinspired material approaches to sensing," Adv. Funct. Mater. 19, 2527 – 2544, 2009.

[28] S. Bauer et al., 25th Anniversary Article, "A Soft Future: From Robots and Sensor Skin to Energy Harvesters," Adv. Mater. 26, 149–162 (2014).

[29] C. Majidi, "Soft Robotics: A Perspective—Current Trends and Prospects for the Future," Soft Robot. 1, 5-11 (2014).

[30] C. Laschi and M. Cianchetti, "Soft robotics: new perspectives for robot bodyware and control," Bionics Biomim. 2, 3 (2014).

[31] E. T. Roche et al., "A Bioinspired Soft Actuated Material," Adv. Mater. 26, 1200–1206 (2014).

[32] R. V. Martinez et al., "Robotic Tentacles with Three-Dimensional Mobility Based on Flexible Elastomers," Adv. Mater. 25, 205–212 (2013).

[33] A. D. Marchese, R. K. Katzschmann, and D. Rus, "Whole arm planning for a soft and highly compliant 2D robotic manipulator," In 2014 IEEE/RSJ International Conference on Intelligent Robots and Systems (IROS 2014) 554–560 (2014). doi:10.1109/ IROS.2014.6942614

[34] B. Mosadegh et al., "Pneumatic Networks for Soft Robotics that Actuate Rapidly," Adv. Funct. Mater. 24, 2163–2170 (2014).

[35] M. T. Tolley et al., "A Resilient, Untethered Soft Robot," Soft Robot. 1, 213–223 (2014).

[36] C. Bergeles and G.-Z. Yang, "From Passive Tool Holders to Microsurgeons: Safer, Smaller, Smarter Surgical Robots," IEEE Trans. Biomed. Eng. 61, 1565–1576 (2014).

[37] V. Vitiello, S.-L. Lee, T. P. Cundy, and G.-Z. Yang, "Emerging robotic platforms for minimally invasive surgery," IEEE Rev. Biomed. Eng. 6, 111–126 (2013).

[38] S. Fusco et al., "An Integrated Microrobotic Platform for On-Demand, Targeted Therapeutic Interventions," Adv. Mater. 26, 952–957 (2014).

[39] J.-P. Hubschman et al., " 'The Microhand': a new concept of micro-forceps for ocular robotic surgery," Eye 24, 364–367 (2010).

[40] Y. Watanabe et al., "Small, soft, and safe microactuator for retinal pigment epithelium transplantation," in IEEE 20th International Conference on Micro Electro Mechanical Systems, 2007. MEMS 659–662 (2007). doi:10.1109/MEMSYS.2007.4433083

[41] S. Wakimoto, K. Suzumori, and K. Ogura, "Miniature Pneumatic Curling Rubber Actuator Generating Bidirectional Motion with One Air-Supply Tube," Adv. Robot. 25, 1311–1330 (2011).

[42] S. Shimomura et al., "Pinching and releasing of cellular aggregate by microfingers using PDMS pneumatic balloon actuators," In 2014 IEEE 27th International Conference on Micro Electro Mechanical Systems (MEMS) 925–926 (2014). doi:10.1109/ MEMSYS.2014.6765793

[43] M. Ikeuchi and K. Ikuta, "in Micro Electronic and Mechanical Systems (Takahata, K. ed.) ," DOI: 10.5772/7000 (InTech, 2009). At http://www.intechopen.com/books/micro-electronic-and-mechanical-systems/membrane-micro-emboss-meme-process-for-3-d-membrane-microdevice, March 17, 2015.

[44] O. C. Jeong and S. Konishi, "All PDMS pneumatic microfinger with bidirectional motion and its application," J. Microelectromechanical Syst. 15, 896–903 (2006).

[45] Y. Jia and Q. Xu, "MEMS Microgripper Actuators and Sensors: The State-of-the-Art Survey," Recent Pat. Mech. Eng. 6, 132–142 (2013).

[46] S. Konishi et al., "Pneumatic micro hand and miniaturized parallel link robot for micro manipulation robot system," in Proceedings 2006 IEEE International Conference on Robotics and Automation, 2006. ICRA 2006 1036–1041 (2006). doi:10.1109/ ROBOT.2006.1641846

[47] W. Wu, A. DeConinck and J. A. Lewis, "Omnidirectional Printing of 3D Microvascular Networks," Adv. Mater., 2011, 23, H178–H183.

[48] M. K. S. Verma, A. Majumder and A. Ghatak, "Embedded Template-Assisted Fabrication of Complex Microchannels in PDMS and Design of a Microfluidic Adhesive," Langmuir, 2006, 22, 10291–10295.

[49] Y. Jia, J. Jiang, X. Ma, Y. Li, H. Huang, K. Cai, S. Cai and Y. Wu, "PDMS microchannel fabrication technique based on microwire-molding," Chin. Sci. Bull., 2008, 53, 3928–3936.

[50] S.-H. Song, C.-K. Lee, T.-J. Kim, I. Shin, S.-C. Jun and H.-I. Jung, "A rapid and simple fabrication method for 3-dimensional circular microfluidic channel using metal wire removal process," Microfluid. Nanofluid., 2010, 9, 533–540.

[51] A. P. Esser-Kahn, P. R. Thakre, H. Dong, J. F. Patrick, V. K. Vlasko-Vlasov, N. R. Sottos, J. S. Moore and S. R. White, "Three-Dimensional Microvascular Fiber-Reinforced Composites," Adv. Mater., 2011, 23, 3654–3658.

[52] Y. Du, M. Ghodousi, H. Qi, N. Haas, W. Xiao and A. Khademhosseini, "Sequential assembly of cell-laden hydrogel constructs to engineer vascular-like microchannels," Biotechnol. Bioeng., 2011, 108, 1693–1703.

[53] C. Xia and N. X. Fang, "3D microfabricated bioreactor with capillaries," Biomed. Microdevices, 2009, 11, 1309–1315.

[54] J. M. Rosano, N. Tousi, R. C. Scott, B. Krynska, V. Rizzo, B. Prabhakarpandian, K. Pant, S. Sundaram and M. F. Kiani, "A physiologically realistic in vitro model of microvascular networks," Biomed. Microdevices, 2009, 11, 1051–1057.

[55] S. Zhao, X. Xu, A. Hughes, S. Thom, A. Stanton, B. Ariff and Q. Long, "Blood flow and vessel mechanics in a physiologically realistic model of a human carotid arterial bifurcation," J. Biomech., 2000, 33, 975–984.

[56] S. Grobe, W. Schroder, and C. Brucker, "Nano-newton drag sensor based on flexible micro-pillars," Meas. Sci. Tech. 17, 2689 – 2697, 2006.

[57] S. Grobe, T. Soodt, and W. Schroder, "Dynamic calibration technique for the micro-pillar shear-stress sensor MPS^3" Meas. Sci. Tech. 19, 105201, 2008.

[58] E. P. Gnanamanickam and J. P. Sullivan, "Manufacture of high aspect ratio micro-pillar wall shear stress sensor arrays," J. Micromech. Microeng. 22, 125015, 2012.

[59] Q. Cheng, Z. Sun, G. A. Meininger, and M. Almasari, "Note: Mechanical study of micromechanical polydimethylsiloxane elastic microposts," Rev. Sci. Instrum. 81, 106104, 2010.

[60] P. Roca-Cusachs, F. Rico, E. Martínez, J. Toset, R. Farré, and D. Navajas, "Stability of Microfabricated High Aspect Ratio Structures in Poly(dimethylsiloxane)," Langmuir, 21, 5542-5548, 2005.

[61] A. De Greef, P. Lambert, and A. Delchambre, "Towards flexible medical instruments: Review of flexible fluidic actuators," Precis. Eng. 33, 311–321 (2009).

[62] M. De Volder and D. Reynaerts, "Pneumatic and hydraulic microactuators: a review," J. Micromechanics Microengineering 20, 043001 (2010)

[63] B. Gorissen et al., "Flexible pneumatic twisting actuators and their application to tilting micromirrors," Sens. Actuators Phys. 216, 426–431 (2014).

[64] B. Gorissen, W. Vincentie, F. Al-Bender, D. Reynaerts, and M. De Volder, "Modeling and bonding-free fabrication of flexible fluidic microactuators with a bending motion," J. Micromechanics Microengineering 23, 045012 (2013).

[65] L. M. Bellan, S. P. Singh, P. W. Henderson, T. J. Porri, H. G. Craighead and J. A. Spector, "Fabrication of an artificial 3-dimensional vascular network using sacrificial sugar structures," Soft Matter, 2009, 5, 1354– 1357.

[66] J. Li, T. A. Rickett and R. Shi, "Biomimetic Nerve Scaffolds with Aligned Intraluminal Microchannels: A "Sweet" Approach to Tissue Engineering," Langmuir, 2009, 25, 1813– 1817.

[67] H. Zhu, S. O. Isikman, O. Mudanyali, A. Greenbaum, and A. Ozcan, "Optical imaging techniques for point-of-care diagnostics," *Lab. Chip*, vol. 13, no. 1, pp. 51–67, Nov. 2012.

[68] X. Mao and T. J. Huang, "Microfluidic diagnostics for the developing world," *Lab. Chip*, vol. 12, no. 8, pp. 1412–1416, Apr. 2012.

[69] J. T. C. Liu, N. O. Loewke, M. J. Mandella, R. M. Levenson, J. M. Crawford, and C. H. Contag, "Point-of-care pathology with miniature microscopes," *Anal. Cell. Pathol. Amst.*, vol. 34, no. 3, pp. 81–98, 2011.

[70] Y. Zhao, Z. S. Stratton, F. Guo, M. I. Lapsley, C. Y. Chan, S.-C. S. Lin, and T. J. Huang, "Optofluidic imaging: now and beyond," *Lab. Chip*, vol. 13, no. 1, pp. 17–24, Jan. 2013.

[71] Z. J. Smith, K. Chu, A. R. Espenson, M. Rahimzadeh, A. Gryshuk, M. Molinaro, D. M. Dwyre, S. Lane, D. Matthews, and S. Wachsmann-Hogiu, "Cell-Phone-Based Platform for Biomedical Device Development and Education Applications," *PLoS ONE*, vol. 6, no. 3, p. e17150, Mar. 2011.

[72] H. Zhu, I. Sencan, J. Wong, S. Dimitrov, D. Tseng, K. Nagashima, and A. Ozcan, "Cost-effective and rapid blood analysis on a cell-phone," *Lab. Chip*, vol. 13, no. 7, pp. 1282–1288, Apr. 2013.

[73] S. B. Kim, K. Koo, H. Bae, M. R. Dokmeci, G. A. Hamilton, A. Bahinski, S. M. Kim, D. E. Ingber, and A. Khademhosseini, "A mini-microscope for in situ monitoring of cells," *Lab. Chip*, vol. 12, no. 20, pp. 3976–3982, Oct. 2012.

[74] T.-F. Wu, T. M. Yen, Y. Han, Y.-J. Chiu, E. Y.-S. Lin, and Y.-H. Lo, "Light sheet microscope compatible with mobile devices for label-free intracellular imaging and biosensing," *Lab. Chip*, May 2014.

[75] B. McCall, M. Pierce, E. A. Graviss, R. Richards-Kortum, and T. Tkaczyk, "Toward a low-cost compact array microscopy platform for detection of tuberculosis," *Tuberc. Edinb. Scotl.*, vol. 91 Suppl 1, pp. S54–60, Dec. 2011.

[76] K. Koo, S. B. Kim, K. Kim, and J. Oh, "An optical multi-sensing system for detection of cardiovascular toxicity," *Biotechnol. Lett.*, vol. 36, no. 5, pp. 1089–1094, May 2014.

[77] J. Lim, P. Gruner, M. Konrad, and J.-C. Baret, "Micro-optical lens array for fluorescence detection in droplet-based microfluidics," *Lab. Chip*, vol. 13, no. 8, pp. 1472–1475, Mar. 2013.

[78] A. Mohan, G. Woo, S. Hiura, Q. Smithwick, and R. Raskar, "Bokode: Imperceptible Visual Tags for Camera Based Interaction from a Distance," in *ACM SIGGRAPH 2009 Papers*, New York, NY, USA, 2009, pp. 98:1–98:8.

[79] A. Arpa, G. Wetzstein, D. Lanman, and R. Raskar, "Single lens off-chip cellphone microscopy," in *2012 IEEE Computer Society Conference on Computer Vision and Pattern Recognition Workshops (CVPRW)*, 2012, pp. 23–28.

[80] J. Lee, J. Paek, and J. Kim, "Sucrose-based fabrication of 3D-networked, cylindrical microfluidic channels for rapid prototyping of lab-on-a-chip and vaso-mimetic devices," *Lab. Chip*, vol. 12, no. 15, pp. 2638–2642, Jul. 2012.

[81] A. S. Nain, J. C. Wong, C. Amon, and M. Sitti, "Drawing suspended polymer micro-nanofibers using glass micropipettes," Applied Physics Letters 89, 183105 (2006).

[82] S. A. Harfenist, S. D. Cambron, E. W. Nelson, S. M. Berry, A. W. Isham, M. M. Crain, K. M. Walsh, R. S. Keynton, and R. W. Cohn, "Direct Drawing of Suspended Filamentary Micro- and Nanostructures from Liquid Polymers," Nano Lett. 4, 1931-1937 (2004).

[83] X. Xing, Y. Wang, and B. Li, "Nanofibers drawing and nanodevices assembly in poly(trimethylene terephthalate)," Opt. Express 16, 10815-10822 (2008).

[84] G. L. Spina, C. Stefanini, A. Menciassi, and P. A. Dario, "novel technological process for fabricating micro-tips for biomimetic adhesion," J. Micromech. Microeng. 15, 1576-1587 (2005).

[85] L. L. Lebel, B. Aissa, M. A. E. Khakani, and D. Therriault, "Ultraviolet-Assisted Direct-Write Fabrication of Carbon Nanotube/Polymer Nanocomposite Microcoils," Advanced Materials 22, 592-596 (2010).

[86] K. Lee, H. C. Lee, D. –S. Lee, and H. Jung, "Drawing Lithography: Three-Dimensional Fabrication of an Ultrahigh-Aspect-Ratio Microneedle," Advanced Materials 22, 483-486 (2010).

[87] M. Prakash and J. W. M. Bush, "Interfacial propulsion by directional adhesion," International Journal of Non-Linear Mechanics 46, 607-615 (2011).

[88] H. Ma, A. K. –Y. Jen, and L. R. Dalton, "Polymer-Based Optical Waveguides: Materials, Processing, and Devices," Advanced Materials 14, 1339-1365 (2002).

[89] C. Zhang, Y. S. Zhao, and J. Yao, "Optical waveguides at micro/nanoscale based on functional small organic molecules," Physical Chemistry Chemical Physics 13, 9060-9073 (2011).

[90] J. R. Pratt, J. A. Kramar, D. B. Newell, and D. T. Smith, "Review of SI traceable force metrology for instrumented indentation and atomic force microscopy," Meas. Sci. Technol. 16, 2129-2137 (2005).

[91] R. S. Gates and J. R. Pratt, "Accurate and precise calibration of AFM cantilever spring constants using laser Doppler vibrometry," Nanotechnology 23, 375702 (2012).

[92] F. M. Sasoglu, A. J. Bohl, and B. E. Layton, "Design and microfabrication of a high-aspect-ratio PDMS microbeam array for parallel nanonewton force measurement and protein printing," J. Micromech. Microeng. 17, 623-632 (2007).

[93] M. Silva-López, A. Fender, W. N. MacPherson, J. S. Barton, J. D. C. Jones, D. Zhao, H. Dobb, D. J. Webb, L. Zhang, and I. Bennion, "Strain and temperature sensitivity of a single-mode polymer optical fiber," Opt. Lett. 30, 3129-3131 (2005).

[94] K. E. Bisshopp and D. C. Drucker, "Large deflections of cantilever beams," Q. Appl. Math. 3, 272-275 (1945).

[95] Y. Xiang and D. A. LaVan, "Analysis of soft cantilevers as force transducers," Applied Physics Letters 90, 133901 (2007).

[96] W. Xu, N. Chahine, and T. Sulchek, "Extreme hardening of PDMS thin films due to high compressive strain and confined thickness," Langmuir 27, 8470-8477 (2011).

[97] D. Fuard, T. Tzvetkova-Chevolleau, S. Decossas, P. Tracqui, and P. Schiavone, "Optimization of poly-di-methyl-siloxane (PDMS) substrates for studying cellular adhesion and motility," Microelectron. Eng. 85, 1289-1293 (2008).

[98] C. Brücker, D. Bauer, and H. Chaves, "Dynamic response of micro-pillar sensors measuring fluctuating wall-shear-stress," Experiments in Fluids 42, 737-749 (2007).

[99] C. Brücker, J. Spatz, and W. Schröder, "Feasibility study of wall shear stress imaging using microstructured surfaces with flexible micropillars," Experiments in Fluids 39, 464-474 (2005).

[100] B. T. Dickinson, "Hair receptor sensitivity to changes in laminar boundary layer shape," Bioinspir. Biomim. 5, 016002 (2010).

[101] E. Jampole, N. Spurgeon, T. Avant, and K. Farinholt, in Topics in Modal Analysis II, Volume 6 (Allemang, R., Clerck, J. D., Niezrecki, C. & Blough, J. R.) 137-152 (Springer New York, 2012).

[102] J. Tao and X. Yu (Bill), "Hair flow sensors: from bio-inspiration to bio-mimicking—a review," Smart Mater. Struct. 21, 113001 (2012).

[103] X. Dou, X. Wang, H. Huang, X. Lin, D. Ding, D. Z. Pan, and R. T. Chen, "Polymeric waveguides with embedded micro-mirrors formed by Metallic Hard Mold," Opt. Express 18, 378-385 (2010).

[104] S. Kim, C. Laschi, and B. Trimmer, "Soft robotics: a bioinspired evolution in robotics," Trends Biotechnol. 31, 287–294 (2013).

[105] D. Trivedi, C. D. Rahn, W. M. Kier, and I. D. Walker, "Soft Robotics: Biological Inspiration, State of the Art, and Future Research," Appl Bionics Biomech. 5, 99–117 (2008).

[106] L. Yao et al., "PneUI: Pneumatically Actuated Soft Composite Materials for Shape Changing Interfaces," in Proceedings of the 26th Annual ACM Symposium on User Interface Software and Technology 13–22 (ACM, 2013). doi:10.1145/2501988.2502037

[107] J. –H. Low, I. Delgado-Martinez, and C.-H. Yeow, "Customizable Soft Pneumatic Chamber–Gripper Devices for Delicate Surgical Manipulation," J. Med. Devices 8, 044504 (2014).

[108] S. Grilli et al., "3D lithography by rapid curing of the liquid instabilities at nanoscale," Proc. Natl. Acad. Sci. U. S. A. 108, 15106–15111 (2011).

[109] J. Paek and J. Kim, "Microsphere-assisted fabrication of high aspect-ratio elastomeric micropillars and waveguides," Nat. Commun. 5, 3324 (2014).

[110] Y. Shapiro, A. Wolf, and K. Gabor, "Bi-bellows: Pneumatic bending actuator," Sens. Actuators Phys. 167, 484–494 (2011).

[111] E. P. Popov, Introduction to Mechanics of Solids. (Prentice-Hall, 1968).

[112] Strength of Materials. (Van Nostrand Company, New York, NY).

[113] S. Konishi, F. Kawai, and P. Cusin, "Thin flexible end-effector using pneumatic balloon actuator," Sens. Actuators Phys. 89, 28–35 (2001).

[114] A. Ghanbari et al., "A micropillar-based on-chip system for continuous force measurement of C. elegans," J. Micromechanics Microengineering 22, 095009 (2012).

[115] H. Rafii-Tari, C. J. Payne, and G.-Z. Yang, "Current and Emerging Robot-Assisted Endovascular Catheterization Technologies: A Review," Ann. Biomed. Eng. 42, 697–715 (2014).